No. C690
May 2022

Optimisation of flight routes for reduced climate impact (OP-FLYKLIM)

Jana Moldanova, Joakim Langner, Magnus Lindskog, Tomas Mårtensson, Michael Priestley, Martin Wall, Ulrika Ziverts, Henrik Ekstrand, Anette Näs, Jens Wilhelmsson

In cooperation with SMHI, FOI, LFV, Swedavia and Novair

Author: Jana Moldanova, Joakim Langner, Magnus Lindskog, Tomas Mårtensson, Michael Priestley, Martin Wall, Ulrika Ziverts, Henrik Ekstrand, Anette Näs, Jens Wilhelmsson
Funded by: Transport Administration's research and innovation portfolio for aviation and the Swedish Transport Agency
Photographer: Jana Moldanova
Report number C690
ISBN 978-91-7883-398-6
Edition Only available as PDF for individual printing

IVL Swedish Environmental Research Institute Ltd.
P.O Box 210 60, S-100 31 Stockholm, Sweden
Phone +46-(0)10-7886500 // www.ivl.se

Preface

The project Optimization of flight routes for reduced climate impact OP-FLYKLIM, which is funded by the Swedish Transport Administration's research and innovation portfolio for aviation and by the Swedish Transport Agency, investigates several areas that are important for the possibilities of reducing aviation's climate impact. This report is the output of four operative work packages of the project.

Table of contents

Summary

The OP-FLYKLIM project investigated the potential to reduce the climate impact of aviation through climate optimization of flight routes to reduce the high-altitude effects of aviation with a focus on climate forcing from contrails and contrail cirrus under Scandinavian conditions. We have developed a calculation methodology where areas with potential to form persistent contrails are identified. The duration and climate forcing of contrails and contrail cirrus in these areas are calculated using data from SMHI's meteorological forecast model. Information on the position and climate forcing potential of these areas has been used to quantify climate forcing of flights on selected routes over a period of several months, and to test optimization of route planning for reduced climate effect with the flight planning system used by the airline Novair.

Climate forcing from contrails and contrail cirrus during the flight calculated with the OP-FLYKLIM methodology is compared with calculations of climate forcing from the CO_2 emitted from combustion of the jet fuel. This enables a direct comparison of the climate benefit of avoidance of contrail formation with its fuel penalty. In the future this method could be deployed in flight planning systems to enable climate optimization. The method can also be used in cost-benefit analyses of climate-optimized flight planning.

We have also investigated several issues that are important for route optimization in general and for correct assessment of whether persistent contrails occur. Meteorological models of good quality in terms of forecasts of winds, temperature and humidity at flight altitude is of great importance both for ordinary route planning and for climate optimization. In OP-FLYKLIM, SMHI has tested streaming data from aircraft (so-called Mode-S EHS data) through air traffic control radars and local data receivers directly to their operational forecast model, which showed improved quality of forecasts.

A persistent contrail occurs only if the humidity in the area of the flight is supersaturated relative to ice but is not already containing clouds. In the project, we have thus investigated the distribution of ice-saturated areas across Scandinavia as an average over several years using data from the ECMWF global numerical weather prediction (NWP) model. The results show a quite high potential for the formation of persistent contrails and thus for high-altitude effects in the area. Comparison to published data on the frequency of occurrence of ice supersaturated layers over Sweden and Europe indicate that observations and model data are broadly consistent. However, when comparing to observed relative humidity with respect to ice (RHI) from radiosondes directly it becomes clear that both the ECMWF model and the MetCoOp model used by SMHI for short range forecasts underestimate RHI near the tropopause, where most flights take place.

As an additional means to evaluate the performance of NWP models with respect to ice supersaturation SMHI initiated observations of contrails by their climate observers at measurement stations with manual observations of climate data. The observations were then matched against flights in the area and RHI calculated by the SMHI forecast model to determine if observations of persistent contrails also corresponded to ice supersaturation in the model. In agreement with the evaluation against radiosondes it was found that the NWP model underestimated RHI in connection with observed contrails.

A correct calculation of fuel consumption and emissions during the flight is a prerequisite both for calculating its high-altitude effects and for monitoring of aviation emissions by national and international authorities. In OP-FLYKLIM the fuel consumption calculated with FOI3

methodology, used for the Swedish reporting of the national emissions from aviation to the UNFCCC and other international reporting obligations, has been compared with true fuel consumption obtained from data from the flight data recorder (FDR data) onboard aircraft on several routes. Comparison showed differences below 10% that could be explained by differences between route plans and type of aircraft in the FDR data and the FOI calculation, respectively.

Sammanfattning

OP-FLYKLIM-projektet har undersökt potentialen i att minska klimatpåverkan från flygtrafik genom klimatoptimering av flygrutter för minskning av flygets höghöjdseffekter med fokus på klimatdrivning från kondensationsstrimmor under skandinaviska förhållanden. Vi har tagit fram en beräkningsmetodik som identifierar områden som har potential att bilda kondensationsstrimmor och som beräknar varaktighet och klimatdrivning från strimmor i dessa områden med hjälp av data från SMHIs meteorologiska prognosmodell. Information om position och klimatdrivningspotential i dessa områden har använts för att kvantifiera klimatdrivning av flygningar på valda rutter under en period på flera månader och för att testa optimering av ruttplanering för minskad klimateffekt med hjälp av ett ruttplaneringsverktyg hos flygbolaget NOVAIR.

Klimatdrivning från kondensationsstrimmor under flygningen som beräknas med metodiken i OP-FLYKLIM jämförs med klimatdrivning från CO_2-utsläpp från förbränning av jetbränsle, vilket möjliggör en direkt jämförelse av nyttan av undvikande av områden med potential att bilda persistenta kondensationsstrimmor med ökningen av bränsleförbrukning för den förlängda flygrutten. I framtiden skulle metodiken kunna användas i ruttplaneringssystem för klimatoptimering. Metodiken kan också användas i kostnads-nyttoanalys av klimatoptimering av flygrutter.

Vi har också undersökt flera frågor som är viktiga för ruttoptimering generellt och för att korrekt bedöma när kondensationsstrimmor uppstår. Meteorologiska modeller av god kvalitet när det gäller prognostisering av vindar, temperatur och fuktighet på flyghöjden är av stor vikt både för ordinarie ruttplanering och för klimatoptimering. I OP-FLYKLIM har SMHI testat att strömma information från flygplan (så kallade Mode-S EHS data) genom flygtrafikledningens radarsystem och lokala datamottagare direkt till sin operativa prognosmodell, vilket visade förbättrad kvalitet hos prognoser.

För att en persistent kondensationsstrimma ska kunna uppstå måste luftfuktighet i området där flygplanet flyger vara övermättad i förhållande till is men inte redan innehålla moln. I projektet har vi därför undersökt förekomsten av isövermättade områden över Skandinavien som ett medelvärde över flera år baserat på data från det europiska vädercentret, ECMWFs, globala väderprognosmodell. Resultaten visade relativt stor potential för bildning av kondensationsstrimmor och därmed höghöjdseffekter i området. Jämförelser med publicerade data av observerad frekvens av isövermättade lager över Skandinavien och Europa pekar på att modellen är konsistent med observationerna. Direkta jämförelser av observerad och modellberäknad relativ fuktighet över is (RHI) visar emellertid att både ECMWFs modell och MetCoOP-modellen som SMHI använder för korta prognoser underskattar RHI i närheten av tropopausen där mycket av flygtrafiken uppehåller sig.

Som ytterligare ett sätt att utvärdera väderprognosmodellerna har SMHI initierat observationer av kondensationsstrimmor med hjälp av sina klimatobservatörer vid mätstationer med manuella observationer av klimatdata. Observationerna matchades sedan mot flygningar i området och isövermättnad beräknad av SMHIs prognosmodell för att testa om observationer av persistenta kondensationsstrimmor också korresponderade mot isövermättnad i prognosmodellen. I linje med utvärdering mot radiosonderingar pekar jämförelserna på att prognosmodellen underskattar relativ fuktighet över is i samband med observerade kondensationsstrimmor.

En korrekt beräkning av bränsleförbrukning och emissioner under flygningen är en förutsättning både för beräkning av dess höghöjdseffekter och för nationella och internationella myndigheters uppföljning av flygemissioner. I OP-FLYKLIM har bränsleförbrukning beräknad med FOI3-metodiken som används för Sveriges internationella rapportering av emissioner från flyg, jämförts med den verkliga bränsleförbrukningen som erhållits från flight-data recordern (FDR-data) ombord på flygplanen på flera rutter. Skillnaden i beräknad jämfört med verklig bränsleförbrukning var mindre än 10% och differensen förklaras av skillnader mellan ruttplaner och typ av flygplan i FDR-data respektive FOI-beräkningen.

List of abbreviations

ABO	Aircraft Based Observation
AMDAR	Aircraft Meteorological Data Relay observing system
ATC	Air Traffic Control
CO_{2e}	CO_2-warming-equivalent emissions
ECMWF	European Centre for Medium range Weather Forecasts
EMADDC	European Meteorological Aircraft Derived Data Centre
ERF	Effective Radiative Forcing
FDR	Flight Data Recorder
FL	Flight Level, aircraft's altitude at standard air pressure, expressed in hundreds of feet (30:ies of meters)
GCD	Great Circle Distance
GTP	Global Temperature Potential
GWP	Global Warming Potential
HARMONIE-AROME	Regional numerical weather prediction modelling system run by a number of cooperating countries including Sweden, which is applied at SMHI
ICAO	International Civil Aviation Organisation
IFS	Integrated Forecasting System
IPCC	Intergovernmental Panel for Climate Change
IRF	Instantaneous radiative forcing
ISSL	Ice-supersaturated layer; layer in the atmosphere with air humidity supersaturated with respect to ice.
ISSR	Ice super-saturated region, cloud-free ice-supersaturated layer
LTO (cycle)	Landing and Take-Off cycle; aircraft movement below 3 000 ft altitude
MEPS	MetCoOp Ensemble Prediction System for Northern Europe
MetCoOp	Collaboration for operational numerical weather prediction models between Finnish, Norwegian and Swedish meteorological offices FMI, Met Norway and SMHI
Mode-S EHS data	Selective-mode (Mode-S) Enhanced Surveillance (EHS) reports are broadcasted by aircraft in response to interrogation from Air-traffic control Enhanced Surveillance radars located at airports in some Air-traffic control regions.
MUAC	Maastricht Upper Area Control Centre
NMVOC	Non-methane volatile organic compounds
NWP	Numerical weather prediction
RF	Radiative forcing

RFI	Radiative Forcing Index
RHI	Relative Humidity with respect to Ice
SLCP	Short-Lived Climate forcing Pollutants
TOA	Top of the atmosphere
TS	Swedish Transport Agency
UNCFCCC	United Nations Framework Convention on Climate Change
UTC	Universal coordinated time
WMO	World Meteorological Organisation

IATA airport codes used in the report

Stockholm, Arlanda; Sweden:	ARN
Kiruna; Sweden:	KRN
Amsterdam, Schiphol; Holland:	AMS
Helsinki, Vantaa; Finland:	HEL
Chania; Greece:	CHQ
Hurghada; Egypt:	HRG
Gran Canaria; Spain:	LPA
Madeira, Funchal; Spain:	FNC

Executive summary

The OP-FLYKLIM project investigated potential to reduce the climate impact of aviation through climate optimization of flight routes to reduce the high-altitude effects with focus on climate forcing from contrails and contrail cirrus under Scandinavian conditions. Several aspects of contrail formation were investigated during the project.

An important condition for formation of contrails is the existence of regions in the atmosphere that are ice supersaturated and free of clouds. OP-FLYKLIM has investigated climatology of such areas over Scandinavia as an average over several years using data from the ECMWF global numerical weather prediction (NWP) model. Results showed quite high potential for the formation of persistent contrails and thus for high-altitude effects in the area (Fig. S1). Comparisons to published data on the frequency of occurrence of ice supersaturated layers over Sweden and Europe indicate that observations and model data are broadly consistent. However, when compared to observed relative humidity with respect to ice (RHI) from radiosondes directly it becomes clear that both the ECMWF model and the MetCoOp model used by SMHI for short range forecasts underestimate RHI near the tropopause, where most flights take place.

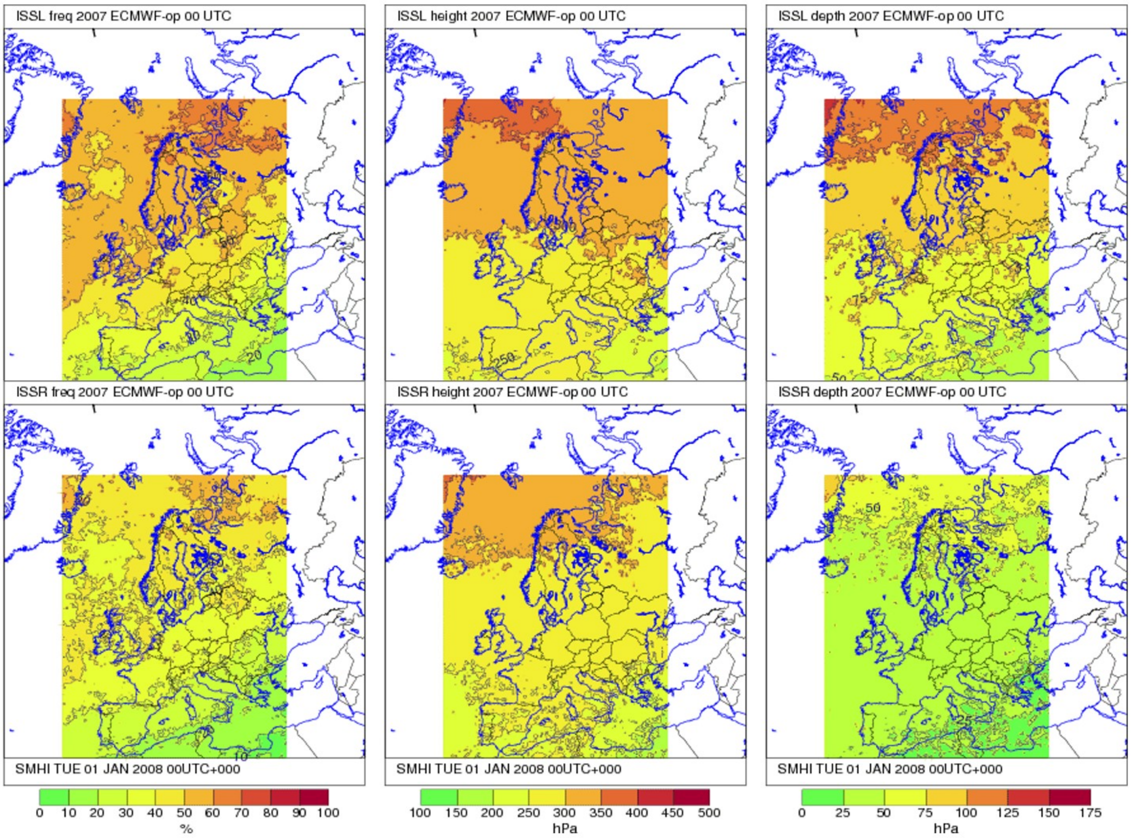

Figure S1. Annual average for 2007 frequency, height, and thickness of ISSL (top row) and ISSR (bottom row) over Europe at 00 UTC derived from operational ECMWF forecasts.

As an additional means to evaluate the performance of NWP models with respect to ice supersaturation SMHI initiated observations of contrails by their climate observers . The observations were then matched against flights in the area and RHI calculated by the SMHI forecast model to determine if observations of persistent contrails also corresponded to ice supersaturation in the model. In agreement with the evaluation against radiosondes it was found that the NWP model underestimated RHI in connection with observed contrails (Fig. S2)

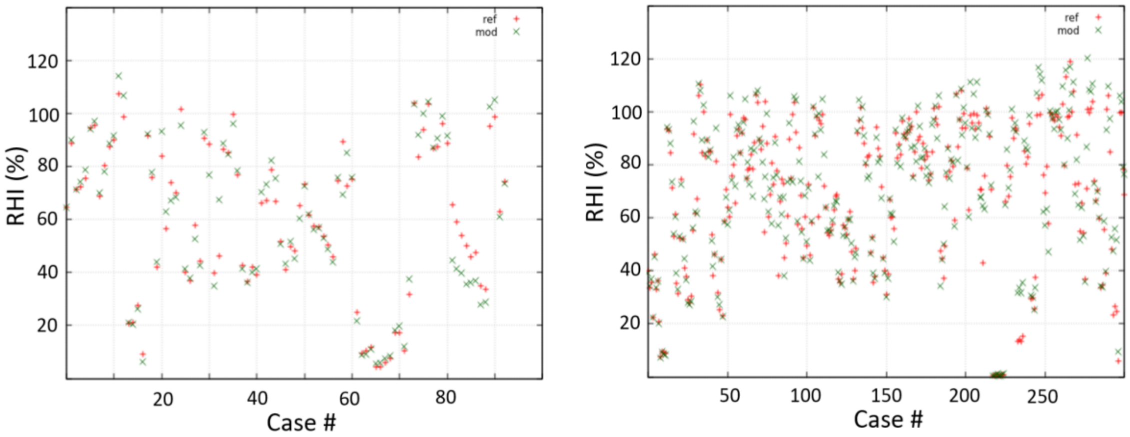

Figure S2. Forecast relative humidity over ice on the vertical axis using reference (red crosses) and modified version (green cross) of the AROME forecast model for observations of contrails during the time periods 1-19 June (left plot) and 2-28 July 2020 (right plot). The horizontal axis indicates the time sequence of the observations. Note that in order to increase the statistical sample 3 or 4 different forecast lengths were compared to each observation. Units: Relative humidity over ice (%).

In aviation meteorological forecasts of good quality in terms of forecasts of winds, temperature and humidity at flight altitude are important for flight planning as well as for studies of climate impact. In OP-FLYKLIM, SMHI has tested streaming data from aircraft (so-called Mode-S EHS data) through air traffic control radars and local data receivers directly to their operational forecast model, which showed an improved quality of the forecasts.

OP-FLYKLIM has developed a methodology to identify ice-supersaturated layers in defined regions and to calculate climate impact of contrails potentially formed in these ISSL based on methodology of Schumann (2012) and Schumann et al. (2012). This methodology is relatively simple and builds on open-source operational meteorological data calculated by the MetCoOp model. The climate impact of contrails and contrail cirrus triggered by a flight was calculated as total energy forcing during their entire lifetime. This energy forcing can be also expressed as CO_2 equivalent and related equivalent mass of jet fuel. OP-FLYKLIM has evaluated impact of individual flights during a three-month period, c.a. 180 evening flights on 2 routes, one between Arlanda, Stockholm (ARN) and Kiruna (KRN) and the second between Helsinki, Vantaa (HEL) and Amsterdam, Schiphol (AMS). For 60% - 65% of the evening flights some polygon with potential of formation of contrails with positive energy forcing occurred in the area, however, only 5-10% of the polygons resulted in radiative forcing of the investigated flights as majority of the polygons was not crossed by the flight route. Fig. S3 shows an example of information on the initial position of ISSL polygons in the region along the route from ARN to KRN and movement of seed-points within these polygons in atmosphere during their entire lifetime as ice-supersaturated. Figure S4 shows the distribution of the ISSL polygons along the Nominal flight route between ARN and KRN in the investigated period of February, March and April 2022. In total, the energy forcing caused by contrail cirrus formed on route ARN-KRN was equal to forcing of CO_2 from 5 350 kg of fuel on a 20-years horizon, which is 1.9% of total fuel consumption. The external costs of the climate forcing of the contrail cirrus, calculated as external cost of climate forcing of equivalent CO_2 emission with unit cost of CO_2-equivalent emission of 50-150 \$/t CO_2 (TWG US Government 2021), was estimated to \$850 -\$2540. For route HEL-AMS the total energy forcing of contrail cirrus corresponded to 1 750 kg fuel and the external cost was \$280 - \$830. Impact of the contrail cirrus during the investigated period was 2% and 0.4% of impact of the fuel on ARN-KRN and HEL-AMS routes, respectively. On the ARN-KRN route 3 flights with highest energy forcing were responsible for 63% of the total EF of the investigated flights on the route. On the HEL-AMS route the 2 flights with the highest energy forcing were responsible for 13%.

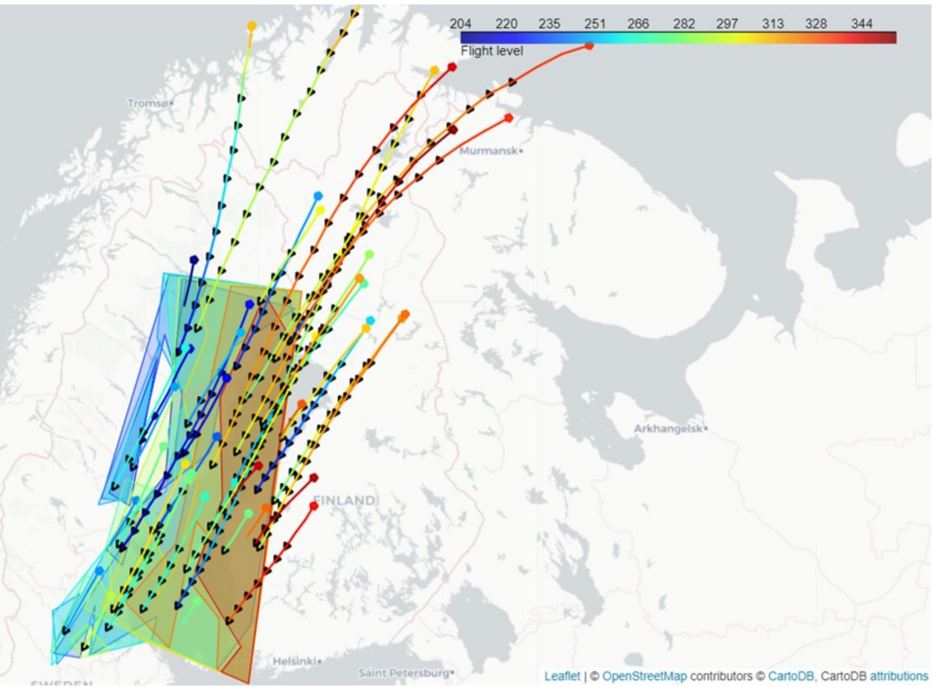

Figure S3. ISSL Polygons with seeds and their fate in the atmosphere calculated along the route between ARN and KRN 2022-02-03. The black triangles show 3-d transport of the seed in an ice-supersaturated atmosphere in 20-min intervals until their endpoint (hexagon) where the atmosphere is not ice-supersaturated. Colour coding shows altitude as flight level (hundreds of feet), both for ISSL polygons, seed transport trajectories and the end-point hexagons.

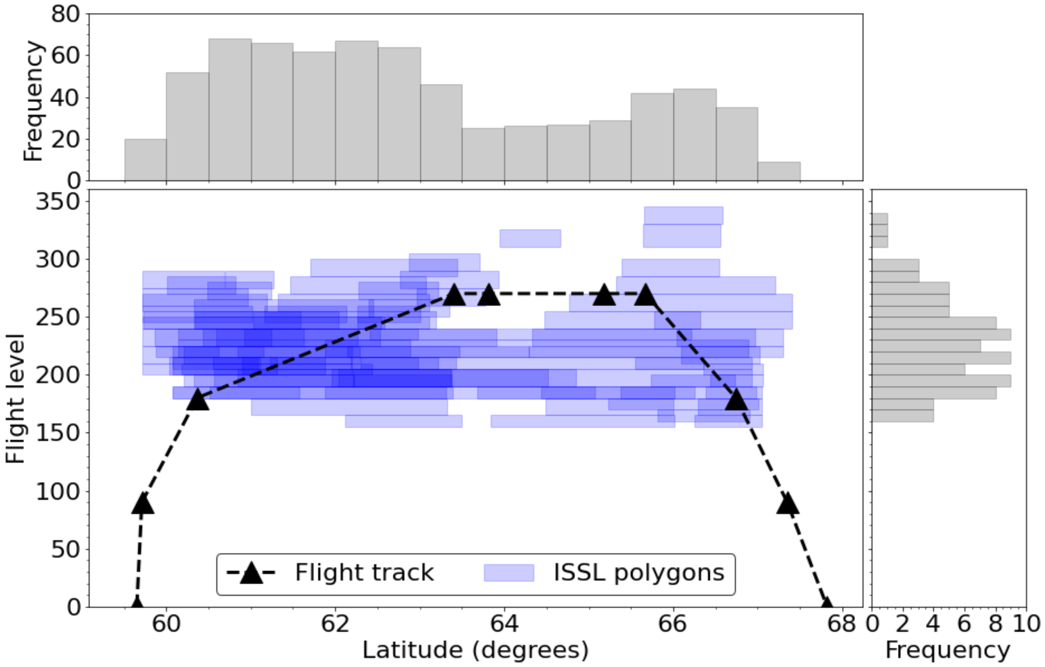

Figure S4. Example flight track for the ARN-KRN route (black triangles are waypoints) including representations of all ISSL polygons (n=741) from the months February, March, and April 2022. The frequency of polygon occurrence in latitude and flight levels (altitude in hundreds of feet) are also shown.

A correct calculation of fuel consumption and emissions during the flight is a prerequisite both for calculating its high-altitude effects and for monitoring of aviation emissions by national and international authorities. In OP-FLYKLIM the fuel consumption calculated with FOI3 methodology, used for national reporting of emissions from aviation, has been compared with true fuel consumption obtained from data from the flight data recorder (FDR data) onboard aircraft on several routes. Comparison showed differences below 10% that could be explained by differences between route plans and type of aircraft in the FDR data and in the FOI calculation, respectively.

1 Introduction

The greenhouse gas (GHG) emissions from the aviation sector and its contribution to global warming has been a subject of intensive discussions in recent years. It is vital to quantify the emissions from aviation and evaluate their climate impact to select the correct measures to lower the climate impact. This type of information is important to create a consensus both for being able to compare the effects of different abatement measures for aviation impact and to be able to relate the impact of aviation to other types of transport.

Today, global air traffic accounts for about 2% of total global anthropogenic emissions of fossil carbon dioxide (CO_2) (Lee et al., 2009, ATAG, 2018). Contribution of aviation to global warming in the form of radiative forcing is, however, larger. Lee et al. (2009) estimated it to be about 4.9% when the impacts of the so-called high-altitude effects are accounted for. These effects are linked to emissions of substances other than CO_2, so-called short-lived climate pollutants (SLCP) including particles, water vapour and nitrogen oxides (NOx), in the upper troposphere. Their impact on the climate is very complex and dependent on local conditions. However, there is a scientific consensus that they have a net warming effect, although it is still difficult to accurately quantify it. It is also dependent on which time perspective and which metrics are applied (Moldanova et al., 2018). Contribution of the high-altitude effects implies that the climate impact of aviation is complex and cannot be directly reduced by simply replacing fossil fuel with renewables.

Current air traffic control systems are affected by a number of international regulations that are often based on conservative calculations and can lead to suboptimal flights in various respects. The regulations are there to safeguard flight safety, which always has the highest priority, and can therefore take a long time to change. New advanced navigation technology in aircraft has great potential to, for example, shorten flight distances. Swedish research is underway within the framework of the IRIS program, where the connection between air traffic control and its system support and air operators with different navigation capabilities must be optimised in the best way. The IRIS program mainly handles the parts of the flight that take place in the vicinity of airports (SID / STAR). The earlier OP-FLYKLIM feasibility study (Moldanova et al., 2018) has shown the possibility of using observations of winds and temperature from the air traffic control system, so-called mode-S EHS data, to improve the results from weather forecast models both in the immediate area of airports and in general in Swedish airspace. Mode-S EHS is flight data that comes via the aircraft transponder. These are available in different designs, and mode-S means that information can be provided from the aircraft to the air traffic control system. EHS (Enhanced Surveillance) means that the aircraft has enhanced its ability to communicate information to the air traffic control system. This information is e.g., speed through the air, its relation to the speed of sound, speed relative to the ground, course and route line etc., which is the basis for calculating e.g., the wind vector and temperature.

Weather data could also be used to optimise flights at higher altitudes, for example with regard to climate impact. Assessing the total climate impact from CO_2, SLCP, contrails and cirrus clouds caused by aviation is complicated, partly due to the fact that these pollutants operate on different time horizons, which requires model systems that span over different temporal and spatial scales. The fact that different pollutants act on different time scales also means that the net effect is different depending on which time horizon is analysed. In addition, the climate effect of many emissions varies depending on the location and the chemical environment in which they occur. In order to reduce the climate impact of aviation, flight routes are primarily optimised, taking into account reduced fuel consumption and thus reduced carbon dioxide emissions, but an optimization could also take into account the high-altitude effects, i.e., effects of SLCP and the formation of contrails and cirrus clouds. Studies of climate optimisation of flight routes avoiding stable ice-supersaturated regions of the atmosphere have shown large potential for reducing the non-CO_2 part of the climate impact of aviation along with relatively small CO_2 trade-offs.

To achieve climate goals with max. 1.5 °C temperature increase, greenhouse gas emissions need to be more than halved by 2050. This goal requires both improved energy efficiency, reduction of the impact of SLCP and a broad transition to alternative (fossil free) fuels. IATA has identified that the use of biojet fuels is the only alternative available for short- and medium-term flights to achieve an emission reduction at that level of ambition. Today, there are a number of certified biojet fuels that are used for aviation, most often as low-grade mixtures. Biojet fuels are also considered to have lower emissions of air pollutants, including particles, than fossil aviation fuels. This property has potential to also reduce their climate impact from contrails and contrail-induced cirrus clouds.

2 Use of air traffic control data and use in numerical weather prediction

(Output of WP3, author: Magnus Lindskog, SMHI)

2.1 Background

Aviation route optimization, for example with respect to Continuous Descent Operation (CDO), is dependent on the quality of the numerical weather forecasts. On the other hand, during the last decade it has been proven in the meteorological community that information from Air Traffic Control (ATC) radar systems located at airports can be used to obtain information of wind speed and air temperature.

Modern aircraft carry sensors to measure the Mach number (using a pitot static probe) and air temperature. In some ATC regions, as an Enhanced Surveillance (EHS) ATC radar interrogates all aircraft in sight in a selective mode, Mode-S Enhanced Surveillance (Mode-S EHS) reports are broadcast by aircraft in response to interrogation from ATC radar. The aircraft replies with a message containing, for example, magnetic heading, airspeed and Mach number. These messages can be collected by ATC or by local receivers. The raw data can be processed to obtain wind and temperature meteorological information. These observations in itself can be useful to the aviation applications in the meteorological community. Furthermore, this information can be used to obtain an improved estimate of the atmospheric forecast model initial state and therefore as well to further improve the forecast quality.

Within this project the plan was to establish a Mode-S EHS stream of raw data from LFV, the Swedish air navigation service provider, to SMHI, to be used in the SMHI kilometre-scale regional operational forecasting system. However, for security reasons at LFV, this did not turn out to be a feasible solution. Therefore, we established and made use of alternative Mode-S EHS data stream solutions. The first step was to use the Numerical Weather Prediction (NWP) model Mode-S EHS data from the Danish ATC radar at Kastrup in Copenhagen and from a local receiver in Oslo. These were processed and made available from the European Meteorological Aircraft Derived Data Centre (EMADDC) in the Netherlands. As a second step we also used data from the part of the Maastricht Upper Area Control Centre (MUAC) Mode-S data that falls into the model NWP domain as well as from Norwegian Defence Research Establishment (FFI). All these data are provided by established data streams. As a third step SMHI has installed a Mode-S receiver station at Arlanda airport that is collecting raw data from the aircraft responses to the Arlanda ATC radar interrogates. These obtained raw data from the receiver are then sent to EMADDC for processing and then the processed data are fetched back to the forecasting system.

Mode-S EHS is one new type of Aircraft Based Observation (ABO) used in NWP models. The most commonly known type of ABO observation traditionally used in NWP models is however probably the global Aircraft Meteorological Data Relay (AMDAR) observing system. This observing system was initiated by the World Meteorological Organisation (WMO) and its members more than thirty years ago, in cooperation with aviation partners. The COVID-19 pandemic was significantly reducing the number of available AMDAR observations from a couple of months into 2020 and to present date.

The regional NWP modelling system applied at SMHI is called HARMONIE-AROME and is run together with a number of cooperating countries within the so-called MetCoOp cooperation. Thanks to this project, the MetCoOp HARMONIE-AROME operational forecasting system is today operationally used. This operational usage was achieved through a number of developments and NWP research experiments where we investigated the characteristics of the Mode-S EHS observations and the impact of these additional observations on the HARMONIE-AROME NWP forecasts.

Methodology and results are summarised below. A more detailed description is given in the attached scientific manuscript, submitted to the Journal of Applied Meteorology.

2.2 Methodology

The Modes-EHS processing chain established is illustrated in Fig. 2.1 below. The local receivers installed at Stockholm Arlanda Airport in Sweden and in Oslo in Norway provide high quality data that are sent to EMADDC. Originally the Oslo receiver was the only source providing Mode-S information from Norway. Today, however, also the Norwegian Defence Research Establishment (FFI) provides data from Norway.

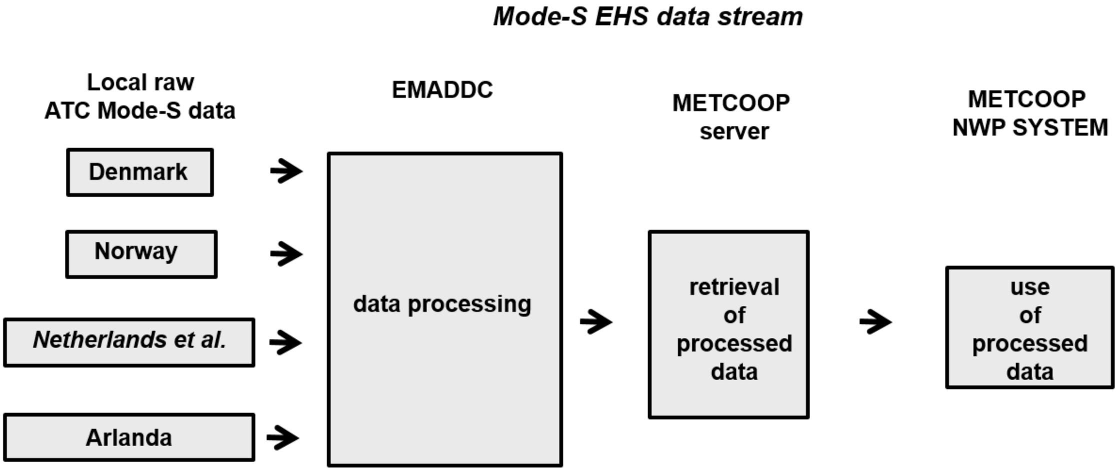

Figure 2.1. Data flow for Modes-EHS used in MetCoOp NWP system.

The location of the Kastrup ATC radar, the Oslo receiver and the Arlanda receiver is shown in Figure 2 below. The grey and the black frames illustrate the horizontal extent of the MetCoOp operational NWP model in 2020 (grey) and 2021 (black).

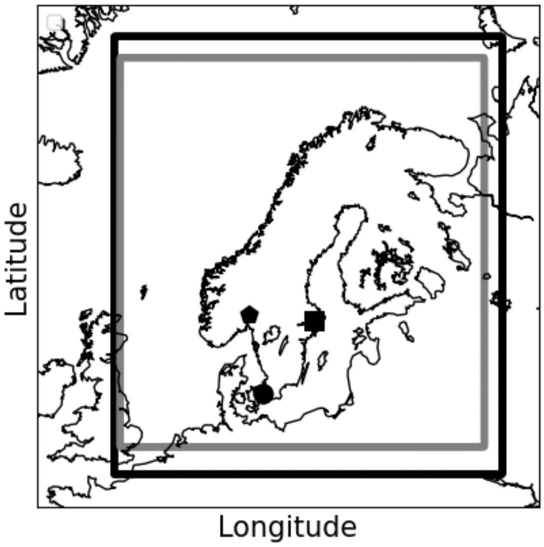

Figure 2.2. Horizontal extent of operationally used MetCoOp domains before (grey) and after (black) domain extension.

The MetCoOp evaluation of Mode-S EHS was done stepwise in two sets of extended parallel experiments. This stepwise approach was a consequence of changes in extension of the MetCoOp model domain and in EMADDC data processing and of a decision to start with evaluation of assimilation of Mode-S EHS observations in parallel. When extending the model domain, more receivers processed by EMADDC were providing Mode-S EHS observations within the new MetCoOp domain. EMADDC had at that time also developed and improved processing of air traffic control data resulting in an improved temperature product (better agreement between modelled and observed temperature). The first set of parallel experiments was carried out for the period 11 December 2019 to 10 January 2020 (from now on referred to as period 1), using a by that time pre-operational version of the MetCoOp HARMONIE-AROME system (cy40), and over the by that time operational domain (grey frame in Fig. 2.2). The two parallel experiments differed only in the use of Mode-S EHS:

- CRL40: A copy of a pre-operational version of the at that time used operational system with operational observation usage.
- EHS40: As in CRL40 but assimilating as well Mode-S EHS wind and temperature data from Denmark and Oslo local receiver.

The second set of parallel experiments were carried out for the period 4 January 2021 to 3 February 2021 (from now on referred to as period 2), again using a pre-operational version of the MetCoOp HARMONIE-AROME system (cy43), and over the currently operational domain (black frame in Fig. 2.2).

- CRL43: A copy of a pre-operational version of the at that time used operational MetCoOp HARMONIE-AROME system with operational observation usage, except for that no Mode-S EHS data are assimilated.
- EHS43: As in CRL43 but assimilating as well Mode-S EHS wind and temperature data.

2.3 Results

In Fig. 2.3, the spatial coverage of assimilated ABO is illustrated for the particular date 19 December 2019 from period 1. The date is chosen to clearly illustrate the typical daily variation in coverage and the differences between Modes-S EHS and AMDAR coverage. It is clear that the number is larger at 12 UTC than at 00 UTC, both for AMDAR and Mode-S EHS. However, for Mode-S EHS the coverage does not vary so much between 00 and 12 UTC. As indicated by the grey dots, both for 00 and 12 UTC cycles, the Mode-S EHS data are confined to the areas around Copenhagen and Oslo. It is clear that it is really AMDAR that provides the coverage over the domain at 12 UTC, whereas there is very little AMDAR data at 00 UTC. Thus, for period 1, during times of the day with many flights the AMDAR data have the attractive feature that they are more evenly distributed over the model area. In Fig. 2.4 the same thing is shown but for 13 January 2021 from period 2. Clearly also for this case there is a clear difference in coverage both for Mode-S EHS and AMDAR between 00 and 12 UTC, with much better coverage at 12 UTC. However, the coverage of Mode-S EHS and AMDAR are quite similar and over many areas complementary.

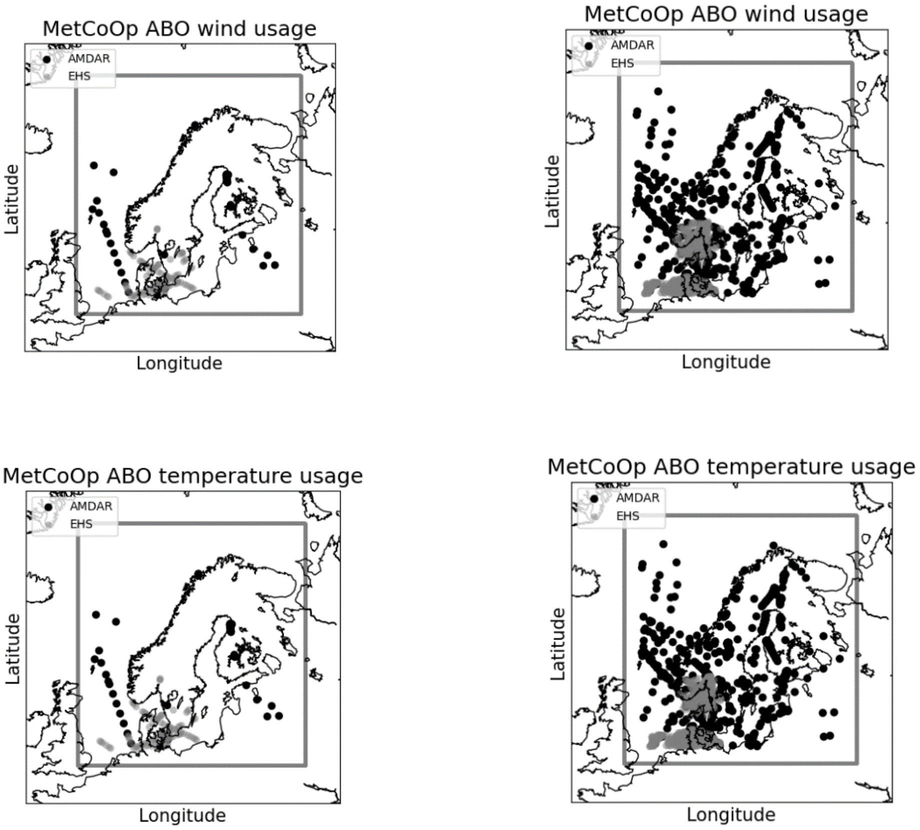

Figure 2.3. Spatial coverage of assimilated ABO from 00 UTC (left column) and 12 UTC (right column) 19 December 2019 (period 1) for wind (upper panel) and temperature (lower panel) observations. Black dots represent AMDAR observations and grey dots Mode-S EHS observations. Grey frame shows the model domain.

Comparing Figs. 2.3 and 2.4 it is obvious that AMDAR coverage has decreased from period 1 compared to period 2 whereas the Mode-S coverage has significantly improved. The reason for the decrease of AMDAR is the pandemic situation with reduced number of flights. The reason for the increase in Mode-S EHS is an extended amount of Mode-S data sources between period 1 and 2. In period 1 only Mode-S data from the Denmark receiver and the Oslo receiver stations were used. For period 2 all Mode-S data sources within the domain that were considered to be of good quality by EMADDC were used. These include data from the Maastricht Upper Area Control Centre (MUAC) ATC's as well as from the Norwegian Defence Research Establishment. The use of Mode-S EHS data thus compensates partly for the reduction of AMDAR data. However, note that there are some parts over the Norwegian sea, the Baltic Sea and Finland for which the coverage has decreased in period 2 compared to period 1. When it comes to the Baltic Sea and Finland the situation will be improved (as seen from the right part of Fig. 2.3) when introducing Mode-S EHS from the Arlanda receiver into the MetCoOp HARMONIE-AROME data assimilation.

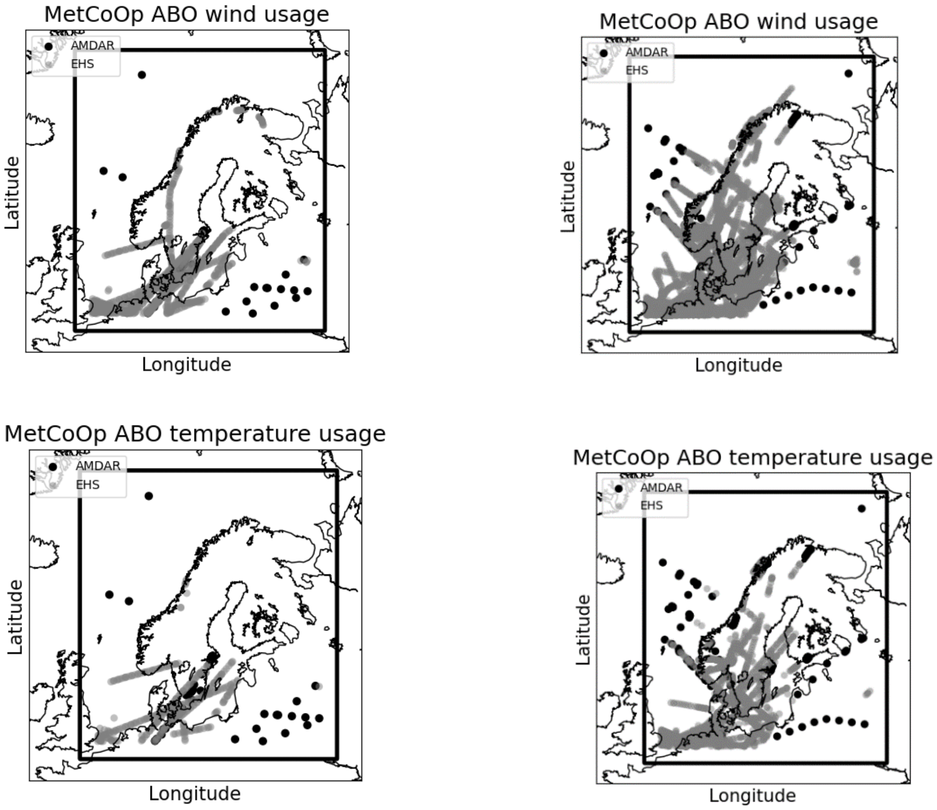

Figure 2.4. Spatial coverage of assimilated ABO from 00 UTC (left column) and 12 UTC (right column) 13 January 2021 (period 2) for wind (upper panel) and temperature (lower panel) observations. Black dots represent AMDAR observations and grey dots Mode-S EHS observations. Grey frame shows the model domain.

The Mode-S EHS data was shown to have a relatively small impact on average forecasts statistics. A neutral to very small impact was found on average verification statistics of MetCoOp wind and temperature forecasts. Encouraging was, however, that a positive impact could be found on individual cases. A key aspect of regional weather forecasting is to provide additional information and improve the forecasts for challenging weather situations. Such improvements are also important for air traffic control. As an illustrative example of such an improvement brought in by the Mode-S EHS data the outcome of a case study is shown below (Figures 2.5-2.7). The prevailing weather condition is a large-scale low-pressure system developing over the North Atlantic and moving toward the west coast of Norway. While this system gradually becomes weaker and moves northward, another frontal system develops in the southern part of the MetCoOp domain and finally a secondary low-pressure system evolves to the north of the Baltic Sea (Fig. 2.5). We provide a case study for these three features where we compare the short-range forecasts between the reference and the mode-s experiments. Figure 2.6 shows the time series of surface pressure at the centre of the low-pressure system. We use the MetCoOp surface analyses as the truth. The comparison between reference and modes indicates that the low centre in the modes is slightly closer to the MetCoOp analysis for +6h forecasts. The same is true when the distance between low pressure centres in MEPS analysis is compared for ref and modes +12h forecasts where the centre in the modes is closer to the MEPS analysis. Figure 2.6 which portrays the tropopause folding over the small cold front shown as a blue curve shows that the use of Mode-S winds shifts the specific humidity minima to a lower level and slightly to the west. This has applications both for the strength and the position of cold front and the subsequent wind and temperature fields if not the precipitation at the surface.

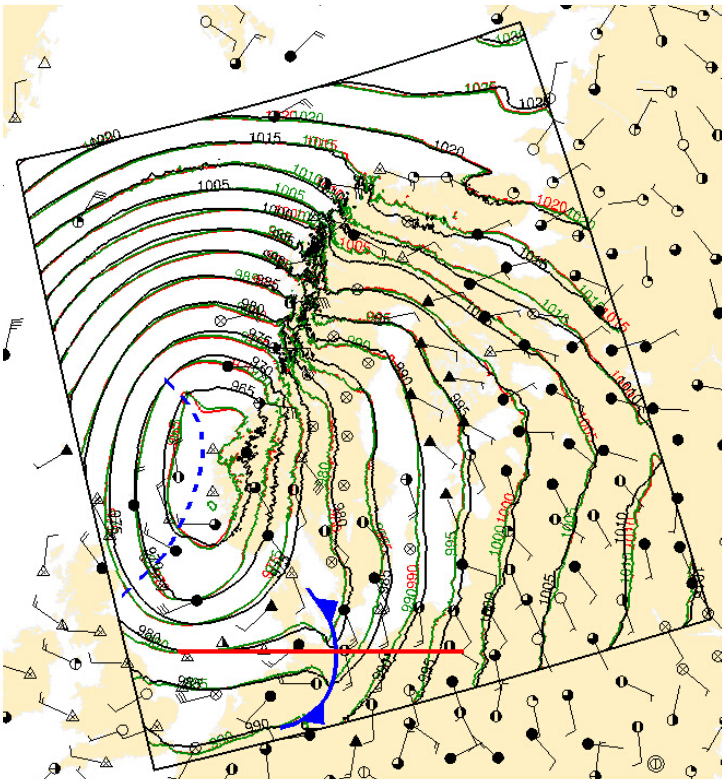

Figure 2.5. Synoptic map at 2021.01.22 06 UTC showing the mean sea level pressure for MEPS analysis (black), reference +18h (green), and modes (red) +18h forecasts every 5 mb. Synoptic stations are also shown in black. The blue dashed line shows the low-pressure trajectory from -24h to +24h moving from south to north. The blue cold front is illustrated in the bottom part of the domain to the east of Denmark. The red line shows the position of cross-section in Figure 2.7.

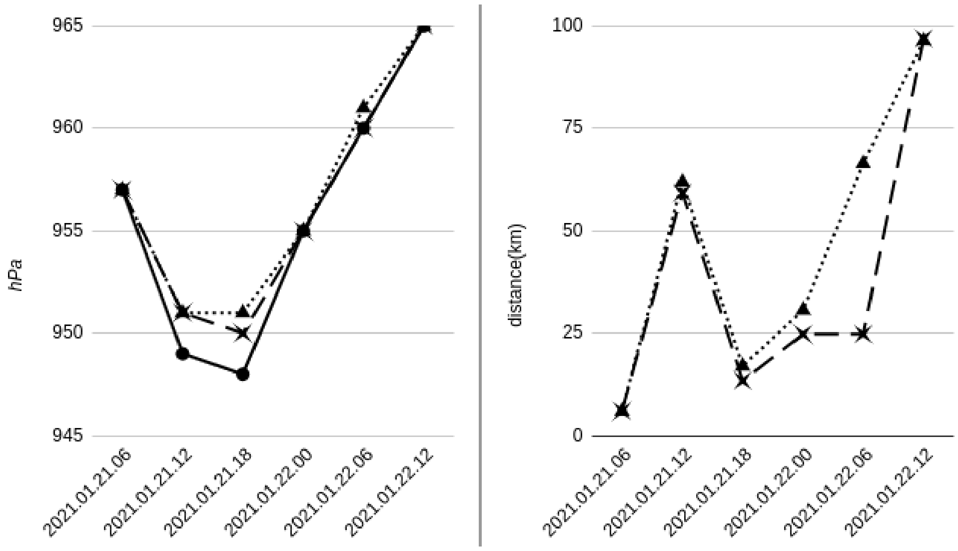

Figure 2.6. Time series of mean sea level pressure at the centre of the low-pressure system (left) for the MetCoOp analysis (solid, circles), reference +6h (dotted, triangles), and modes (dashed, stars) +6h forecasts, and the distance in km between low pressure centres (right) in MEPS analysis against reference (dotted, triangles) +12h forecast and modes (dashed, stars) +12h forecasts.

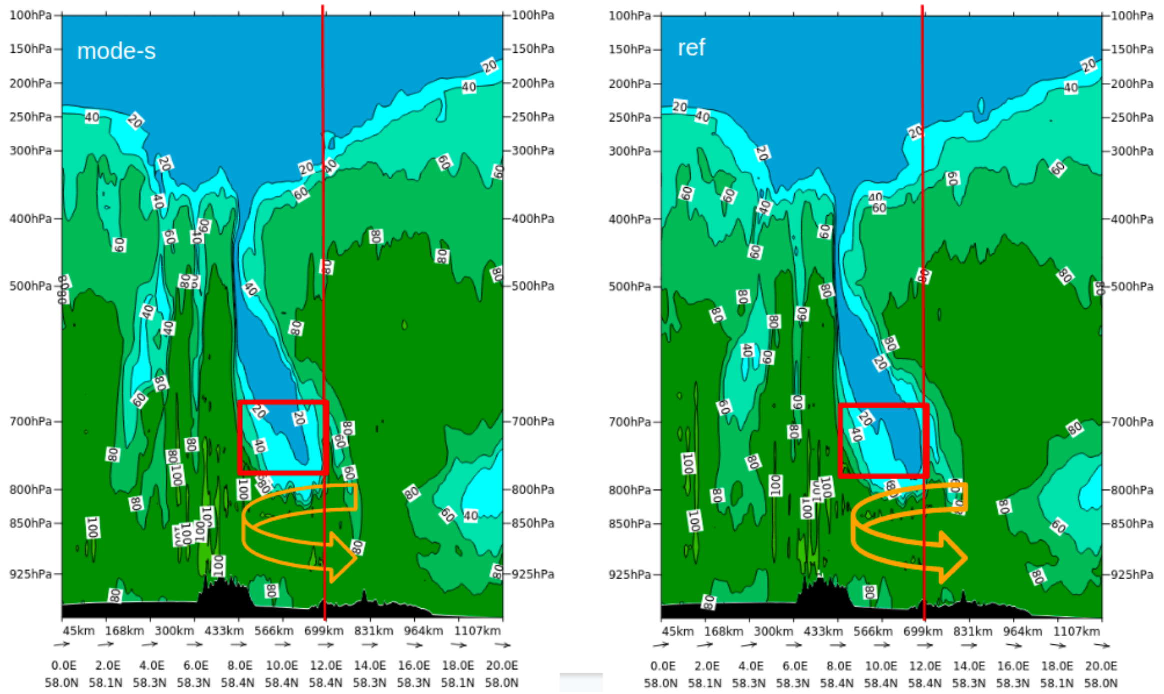

Figure 2.7. Tropopause folding showed with relative humidity cross sections for reference +6h forecast (left) and modes +6h forecast (right). The identical red box and red vertical line in both cross sections indicate that in the modes experiment the maximum dry air at around 800 hPa is shifted slightly upward and westward for the +6h forecast, slightly shifting the cyclonic circulation and the surface front to the west.

Recently an EMADDC data stream including the Arlanda receiver has become available. There is a rather large increase in the number of observations compared to the current operational data stream as shown by Fig. 2.8. The new operational stream, containing the Arlanda receiver as well, installed and evaluated within this project, was introduced for operational use in MetCoOp on 3 May 2022. In Fig. 2.9 and Table 2.1 we demonstrate for one particular day that the quality of Arlanda receiver data is as good as from other Mode-S data sources for comparison against short-range global forecasts from ECMWF.

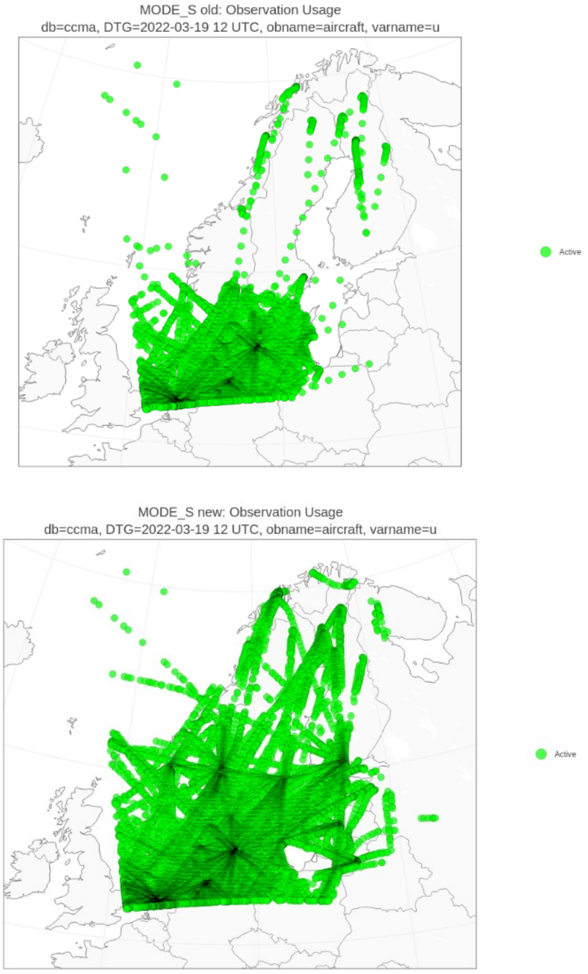

Figure 2.8. Horizontal coverage of the operational data stream (left) in March 2022 compared to the new data stream including the Arlanda receiver (right) at noon.

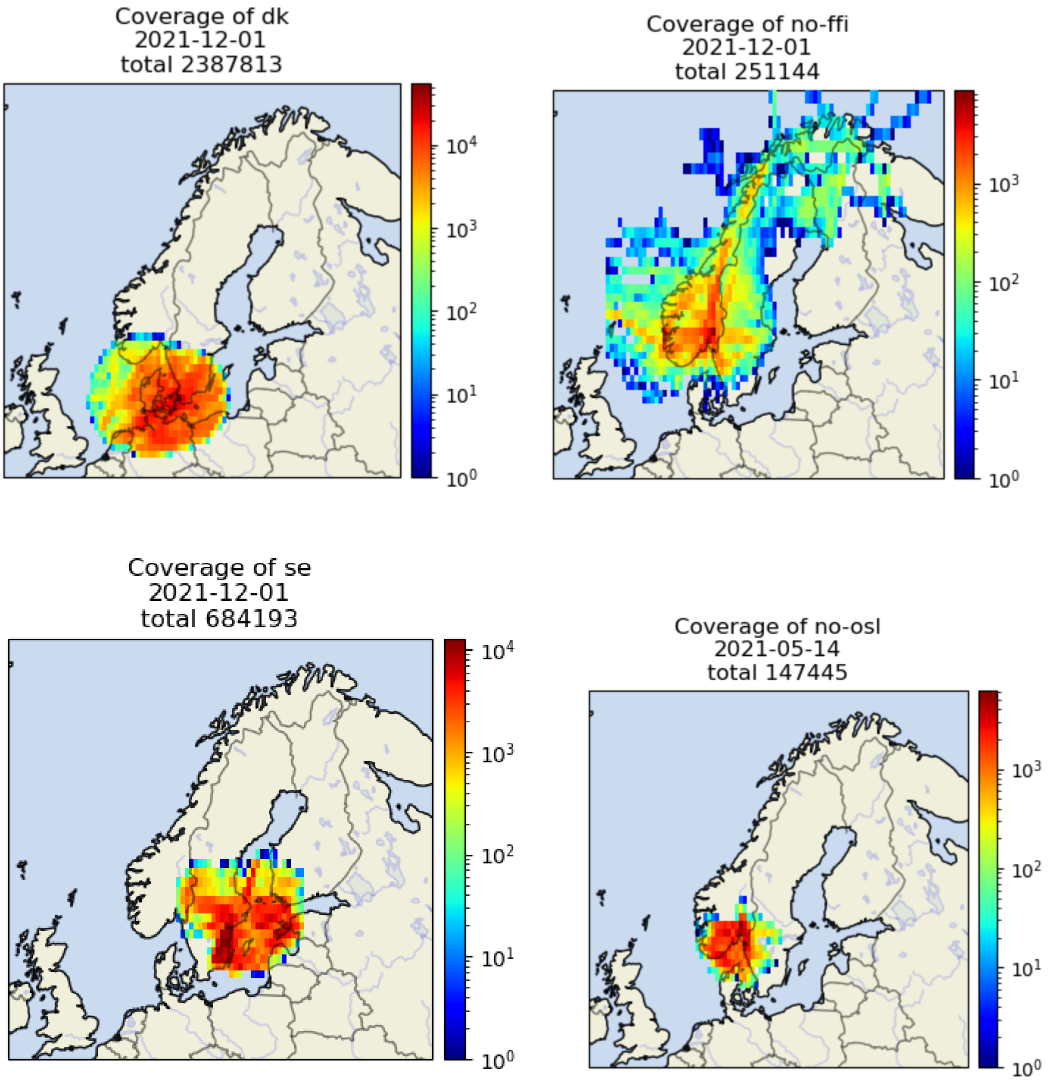

Figure 2.9. Data coverage for the particular days (1 December 2021 and 14 May 2021), as derived from Danish ATC (top left), Norwegian Defence Research Establishment (top right), Arlanda (bottom left) and the Oslo local receiver (bottom right). The colour scale indicates the number of observations in boxes of half a degree.

Table 2.1. Verification statistics of Mode-S EHS data sources against ECMWF forecasts.

source	period	wind speed [m/s]			temperature [K]		
		number	bias	st.dev.	number	bias	st.dev.
dk	2021/01/01 - 2021/12/31	384 216 508	0.26	2.41	319 844 727	0.07	1.03
no	2021/01/01 - 2021/05/11	12 830 463	0.40	2.61	5 115 275	0.01	0.93
no-osl	2021/05/11 - 2021/05/29	359 743	0.53	2.62	179 431	0.05	0.95
no-ffi	2021/07/03 - 2021/12/31	11 400 638	0.29	2.47	7 370 922	0.00	1.00
se	2021/06/07 - 2021/12/31	14 455 283	0.32	2.52	16 384 086	0.03	1.03

2.4 Conclusions

Within this project we have introduced additional important aircraft-based observations into the MetCoOp regional modelling system. It has been demonstrated that these additional aircraft-based observations have partly compensated for the reduced number of aircraft AMDAR observations during the COVID pandemic. The benefit of the data has been demonstrated through a case study, illustrating the importance of Mode-S in significant weather situations. Improved accuracy of weather forecast in such situations is of great importance for both air traffic control and for taking into account simultaneously environmental and security aspects. As a final step in the project, we recently managed to introduce data from the Arlanda receiver into the MetCoOp operational NWP system and demonstrate the quality of this data. We foresee an enhanced use of the Arlanda receiver data in the near future for various aviation meteorology applications and tools in the near future.

3 Fuel consumption and emissions

(Output of WP2; Author: Tomas Mårtensson, FOI)

3.1 Background

When optimising a flight-route in order to reduce contrail formation it is important to quantify how the achieved benefits from changing the route (horizontally and vertically) trades with changes in fuel burn and emissions. FOI has applied different tools in order to quantify fuel consumption and emissions for the different flights used within the OP-FLYKLIM project.

3.2 Methodology

3.2.1 FOI3-method for calculation of emissions

The Swedish Transport Agency (TS) has commissioned the Swedish Defence Research Agency (FOI) to perform the aviation emission calculations for Sweden’s reporting to the United Nations Framework Convention on Climate Change (UNCFCCC). The mentioned calculations are based on FOI3-method (Mårtensson and Hasselrot, 2013). See Figure 3.1 for a work-flow description of the method.

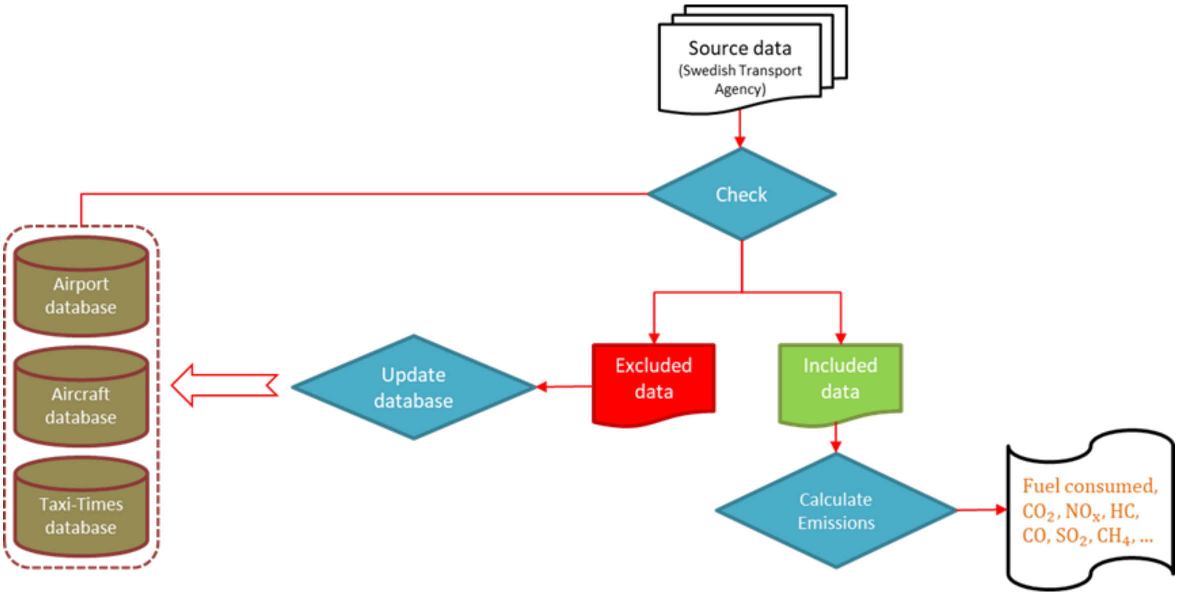

Figure 3.1. An illustration of the workflow running the FOI3-method. Source data is checked in order to flag potentially missing airports or aircraft in the databases. If needed, updates are made accordingly. A flight category check ensures that only intended data is included in the calculations. There are flags for the ICAO categories “Commercial Air Transport Services" and “General Aviation” and their associated subcategories. The Aircraft database is built on data from the commercial software Piano.

The underlying aircraft and engine data comes from the commercial software Piano (www.lisys.uk). Piano contains a database with technical data for +500 aircraft, well covering all relevant aircraft operating in Sweden. For every aircraft type, emissions are calculated for a variety of simplified flight trajectories (high/low and long/short shown in Figure 3.2) where Piano utilises emission factors from ICAO’s engine exhaust emission database (EASA, 2021) as well as other sources. Calculations in Piano are performed at a fixed cabin factor of 65%.

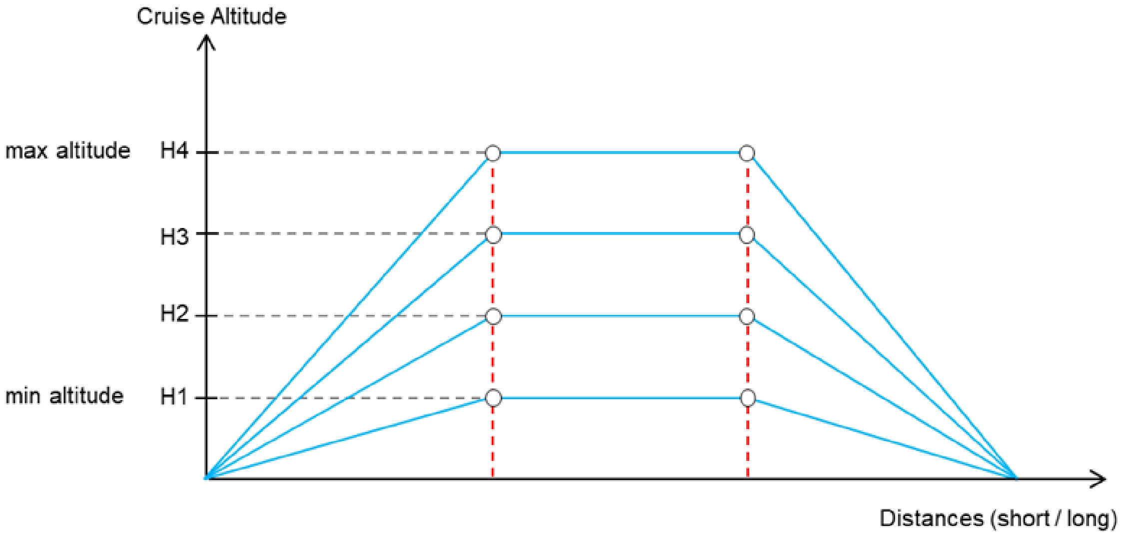

Figure 3.2. Illustration of the data-points calculated with Piano for fuel burn and emissions

The eight data-points derived from Piano go into the FOI3 applications database. All flights are divided into nine segments as shown in Figure 3.3: taxi out, take-off, climb-out (climb to LTO i.e. 3000 ft), climb, cruise, descent, approach (descent from LTO), landing and taxi in. All segments can be studied separately, but normally the whole flight, or the LTO-cycle (below 3000 ft), are automatically summed in the system.

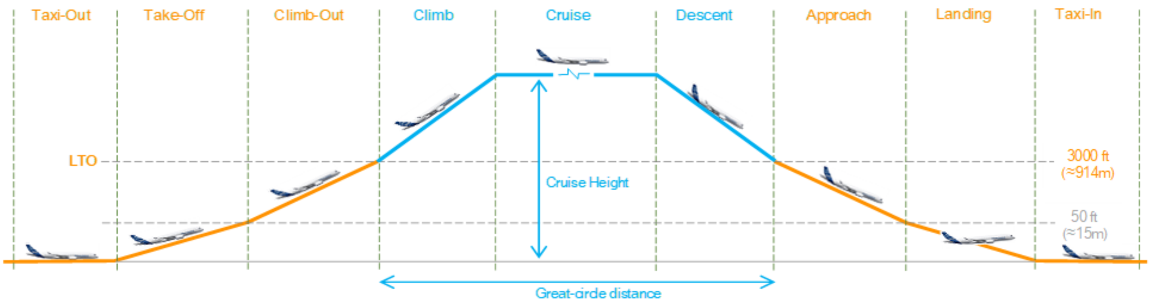

Figure 3.3. Illustration of the nine segments the FOI3 model utilises for emission and fuel burn calculations.

The input data from the Swedish Transport Agency contains aircraft-id, aircraft type, arrival/departure airport, number of passengers and type of flight according to ICAO nomenclature for all international and domestic flights. The FOI3 tool stores the actual mean taxi times reported from Swedish airports in the taxi-time database (as shown in Figure 3.1). The Swedish Transport agency usually provides the data. For international flights, the ICAO-standard taxi times are used. The FOI3 method applies a simple correction for cabin factor, adjusting the fuel burn and emissions up or down depending on the difference between the reported actual cabin factor and the assumed 65%, which the underlying data is based on.

The tool calculates fuel burn and aviation emissions of carbon dioxide (CO_2), carbon monoxide (CO), sulphur dioxide (SO_2), nitrogen oxides (NO_x), methane (CH_4), non-methane volatile organic compounds (NMVOC), and nitrous oxide (N_2O)

The FOI3-method has its limitations. It always uses the great circle distance (GCD) between airports as the flown distance. In an investigation from 2016, where thousands of radar-tracks for domestic traffic were analysed, it was shown that the mean Swedish domestic flights were about 7.8 % longer than the corresponding GCD [Mårtensson et al., 2016]. Eurocontrol publishes this type of data for European air traffic, both cruise segments but also for terminal manoeuvring areas closer to the airports.

The FOI3-database only holds one combination of aircraft and engine. For example, Boeing 737-800, which in reality comes with different seat plans (maximum number of passengers) and different engines, only holds one engine and one seat plan in the FOI3 database. Some effort has been put into selecting and matching the aircraft versions that are most commonly used by the larger airline operators in Sweden.

The FOI3-method defines the cruise altitude in an iterative way. It uses the highest possible cruise altitude for the selected distance since it (in theory) will be the most efficient way to operate in terms of fuel burn. In practice this means that the model usually flies the aircraft at higher altitudes than what is the case in real-life operations, with the difference being larger for short flights.

3.3 Results

3.3.1 Emissions for flights from ARN to CHQ, FNC, HRG and LPA

For those flights, real data (FDR) from Novair’s aircraft Airbus A321-251Neo (A321neo) was provided to the project. In total 25 flights per route. Here the emissions and fuel burn have been calculated both with the FOI3-model and the commercial software Piano. The outcomes are then compared with the mean observed value for the 25 flights.

Some flight records were excluded from the analysis since data was incomplete. In Figure 3.4, all included flights from ARN (Stockholm, Arlanda, Sweden) to LPA (Gran Canaria, Las Palmas, Spain) are illustrated in a 3D-view. There is a clear spread in how the flights actually are routed. No information on the number of passengers is included in the FDR-data, but take-off mass is included. Note that the FDR data does not contain any information on emissions from carbon monoxide (CO), hydrocarbons (HC) or nitrogen oxides (NO_x), this is only provided by the FOI3- and Piano model.

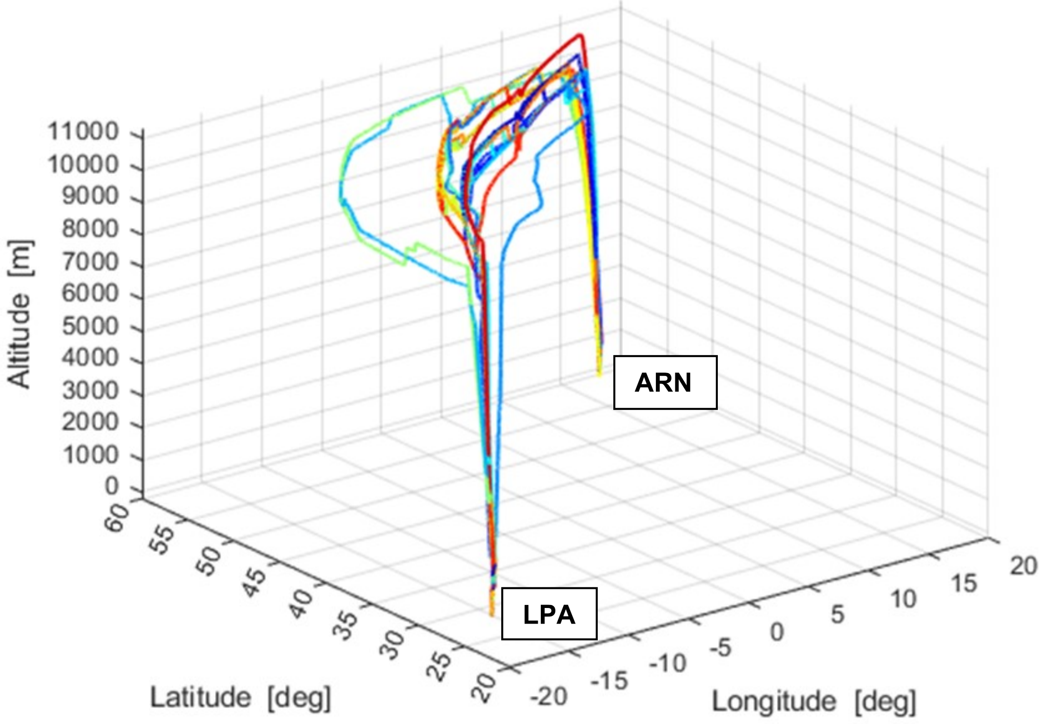

Figure 3.4. A 3D-plot of all 25 flights ARN-LPA. X-axis is longitude (West - East), Y-axis latitude (South to North), Z-axis is altitude [m]. LPA is the point in the lower left corner (closest), ARN upper right. Note that most flights are routed more to the west than the great circle distance between the points, a few flights are significantly re-routed westward.

The Piano model was set up in such a way that the FDR mean distance and cruise altitude were used as input to Piano. Flight time and fuel consumption are calculated output. For the FOI3 model the version of A321-200 used in the calculation has 180 passengers as maximum payload, and a maximum take-off mass of 83 000 kg, A 100% cabin factor was assumed for all calculations (Engine CFM56-5C2)

Differences in calculated total fuel burn for the FOI3-model and Piano are compared with the FDR mean for each city-pair in Table 3.1. For comparison, the flights with lowest and highest fuel consumption within the FDR-dataset are also listed (relative to the mean [%])

As expected, results from Piano are better than the FOI3-model. Both models estimate the fuel consumption well within the natural spread between the real flights. Both models underestimate the fuel consumption for the two longest flights from ARN to Madeira and LPA (ARN-FNC and ARN-LPA). The take-off weight is underestimated for all flights, but most for those two destinations, this is probably the explanation for this result.

Since information on emissions from carbon monoxide (CO), hydrocarbons (HC) or nitrogen oxides (NO_x) only is provided by the FOI3- and Piano model a comparison between those was made. Here it becomes obvious that the Piano model shows much lower emissions. This is expected since the Piano uses data for an engine belonging to the newest generation (CFM Leap-1A) which is used on Novair´s A321neo fleet. The FOI3 model assumes an older engine generation on its version of A321-200 (CFM56-5C2), in summary:

- CO emissions are 52-55 % lower for the Leap-1A engine

- HC emissions are 88-90 % lower for the Leap-1A engine
- NO_x emissions are 29-30 % lower for the Leap-1A engine

Note that the release of carbon dioxide is directly proportional to the fuel burn and hence have the same variations as Table 3.1, while Table 3.2 - Table 3.5 contain a summary with all absolute values.

Table 3.1. Fuel burn comparison. The models FOI3 and Piano compared to the mean value from FDR-files. Last columns show the lowest/highest recorded fuel consumption for one flight within the dataset (relative to the mean).

Flight Route	Nr. of FDR-files used for mean	FOI3 fuel burn (relative FDR mean)	Piano fuel burn (relative FDR mean)	Lowest fuel burn (relative FDR mean)	Highest fuel burn (relative FDR mean)
ARN – CHQ	21	7.4 %	3.7 %	-11 %	8 %
ARN – HRG	25	4.2 %	3.3 %	-8 %	17 %
ARN - LPA	19	-2.8 %	-0.8 %	-8 %	10 %
ARN - FNC	15	-2.5 %	-4.4 %	-12 %	14 %

Table 3.2. Comparative results from FOI3, Piano and FDR-data for the flight route: ARN-CHQ (Chania, Greece). Note that Piano used the mean FDR-values for cruise altitude and distance as input values (pink marking).

ARN-CHQ	FOI3	Piano 3d	FDR mean (21 records)
Weight [kg]	83 000	82 150	78 245
Cruise altitude [m]	11 857	10 820	10 809
Time [min]	228	226	219
Distance 3d [km]	2 748	2 829	2 829
Total fuel [kg]	9 437	9 066	8 739
Total CO [kg]	34.43	15.6	N/A
Total CO_2 [kg]	29 821	28 649	N/A
Total HC [kg]	4.02	0.41	N/A
Total NOx [kg]	132.61	92.6	N/A

Table 3.3. Comparative results from FOI3, Piano and FDR-data for the flight route: ARN-HRG (Hurghada, Egypt). Note that Piano used the mean FDR-values for cruise altitude and distance as input values (pink marking).

ARN-HRG	FOI3	Piano 3d	FDR Mean (25 records)
Weight [kg]	83 000	85 838	85 992
Cruise altitude [m]	11 857	10 668	10 646
Time [min]	308	308	296
Distance 3d [km]	3 839	3 969	3 969
Total fuel [kg]	12 887	12 754	12 347
Total CO [kg]	42.59	20.3	N/A
Total CO_2 [kg]	40 723	40 303	N/A
Total HC [kg]	4.82	0.56	N/A
Total NOx [kg]	179.4	126	N/A

Table 3.4. Comparative results from FOI3, Piano and FDR-data for the flight route: ARN-LPA. Note that Piano used the mean FDR-values for cruise altitude and distance as input values (pink marking).

ARN-LPA	FOI3	Piano 3d	FDR Mean (19 records)
Weight [kg]	83 000	87 671	89 252
Cruise altitude [m]	11 857	10 577	10 589
Time [min]	346	347	351
Distance 3d [km]	4 365	4 518	4 518
Total fuel [kg]	14 562	14 857	14 970
Total CO [kg]	46.52	22.3	N/A
Total CO_2 [kg]	46 015	46 948	N/A
Total HC [kg]	5.21	0.631	N/A
Total NOx [kg]	202.25	143	N/A

Table 3.5. Comparative results from FOI3, Piano and FDR-data for the flight route: ARN-FNC. Note that Piano used the mean FDR-values for cruise altitude and distance as input values (pink marking).

ARN - FNC	FOI3	Piano 3d	FDR Mean (15 records)
Weight [kg]	83 000	86 088	88 481
Cruise altitude [m]	11 857	10 698	10 691
Time [min]	317	313	315
Distance 3d [km]	3 960	4 038	4 038
Total fuel [kg]	13 272	13 004	13 606
Total CO [kg]	43.5	20.4	N/A
Total CO2 [kg]	41 938	41 093	N/A
Total HC [kg]	4.91	0.569	N/A
Total NOx [kg]	184.63	128	N/A

3.3.2 Domestic flight ARN to KRN

The first analysis within the project was to quantify fuel burn and emissions for a few domestic flights ARN-KRN in the northern part of Sweden) with an Airbus A321neo. FOI´s estimates, based only on the FOI3 method, were compared with output data from the flight planning system for this aircraft type. Table 3.6 illustrates the differences between the two tools.

Table 3.6. Comparison between the FOI3-model and the flight planning system for parameters flown time, distance, cruise altitude and total fuel consumption for a flight ARN-KRN for an Airbus A321neo.

ARN-KRN	Time [min]	Distance [km]	Cruise alt [FL]	Fuel [kg]	NOx [kg]	HC [kg]	CO [kg]	CO2 [kg]
FOI3	89	941	389	3 644	55.7	2.1	17.5	11 514
Flight plan	82	989	358	3 273	-	-	-	10 343
Difference in %	**8 %**	**-5 %**	**8 %**	**10 %**	**-**	**-**	**-**	**10 %**

The differences are in the order of 10% or less. Note that the FOI3 model uses an older engine version than the one used in the flight planning system run by Novair. This is the major reason why the fuel burn is higher for the FOI3 method. The FOI3-method inherently uses the highest possible cruise altitude on each flight (see explanation in section above). In this case cruise at 38 900 feet (FOI3), which is 3100 feet higher than flight planning system. This also (in part) explains the longer flight time assumed by the FOI3 method.

4 Climate impact from short lived climate forcing pollutants and contrails

(Output of AP4; Authors: Joakim Langner, Jana Moldanova, Michael Priestley, Jens Wilhelmsson, Karl-Ivar Ivarsson)

4.1 Background

In addition to emissions of fossil CO_2, aviation affects the climate through other mechanisms that involve emissions of water vapour, soot and other particles, formation of contrails and NOx emissions. These other effects are often shortly called high-altitude effects and the radiative-forcing compounds have got a common name short-lived climate forcing pollutants (SLCP). SLCP are emitted by both land-based emission sources, shipping and aviation; effects of SLCPs emitted from aviation are, however, particularly important as their impact in the tropopause region, where most of the aviation emissions occur, is much higher than at the Earth surface. An important reason for this - but not the only one - is that aviation emissions take place above the surface mixed layer, which means that they reside longer in the atmosphere and are not included in the natural water cycle with a fast turnover rate. Below is an overview of processes associated with impact of aviation on climate:

- CO_2 emissions (warming).
- Emissions of water vapour at high altitude (warming).
- NOx emissions leading to ozone formation in the troposphere (warming).
- Emissions of NOx which via atmospheric chemical processes lead to the decomposition of methane in the atmosphere (cooling), which in turn causes a reduction of tropospheric ozone over a long-time horizon (cooling); reduction of methane also leads to reduction of water vapour over the same time horizon (cooling) (Grewe et. al., 2014).
- Emissions of soot particles cause direct positive radiative forcing (warming).
- Formation of sulphate particles from the sulphur in the jet fuel causes direct negative radiative forcing (cooling).
- Formation of persistent contrails after the aircraft contributes with both positive (warming) and negative (cooling) radiative forcing, but the overall effect is positive (warming).
- The formation of cirrus clouds from scattered contrails contributes, like contrails, with both positive and negative radiative forcing with a net warming effect.
- Soot particles from aircraft can affect cirrus clouds also by seeding the clouds, i.e., particles act as extra condensation nuclei for cloud droplets, the magnitude and also the direction of impact of that effect is however very uncertain. A recent study (Kärcher et al., 2021) rules out the importance of this impact.
- Soot particles from aviation contribute to warming also indirectly, through deposition on ice and snow in the Arctic (Jacobsson et al., 2012).

For climate systems that are in equilibrium, i.e., if the concentration of greenhouse gases is constant or increases at a steady rate, a linear relationship between global mean temperature change at the earth's surface ΔTs and radiative forcing perturbation ΔF applies:

$\Delta Ts = \lambda * \Delta F$

Where λ is the climate sensitivity parameter that for long-lived greenhouse gases was earlier assumed to have a constant value (which can differ between different climate models). Later research has shown though that λ varies with the type of radiative forcing, especially if it is inhomogeneous. This also applies to radiative forcing from aviation-related ozone, contrails and cirrus clouds, and a review by Lee et al. (2009) presented differences in climate sensitivity for these aviation-related compounds (*i*) in terms of their efficacies, i.e. ratio $\lambda_i / \lambda_{CO2}$. More recent studies adopted the concept of Effective Radiative Forcing (ERF) where the radiative forcing of the compound is adjusted for changes in the troposphere that occur directly due to the changes in radiative forcing without mediation by the global mean temperature change (Sharewood et al., 2015). Due to this adjustment the climate sensitivity of the system does not differ between the different compounds. Figure 4.1 presents ERF of the different compounds related to emissions from aviation released to the atmosphere between years 1940 and 2018 published in a recent review of Lee et al. (2021). Their estimate of the 2018 ERF from aviation is 100.9 (70 – 229) mW/m^2 (with 5–95% confidence interval) and ERF of aviation CO_2 only (equal to RF) is 66.6 (21 – 11) mW/m^2.

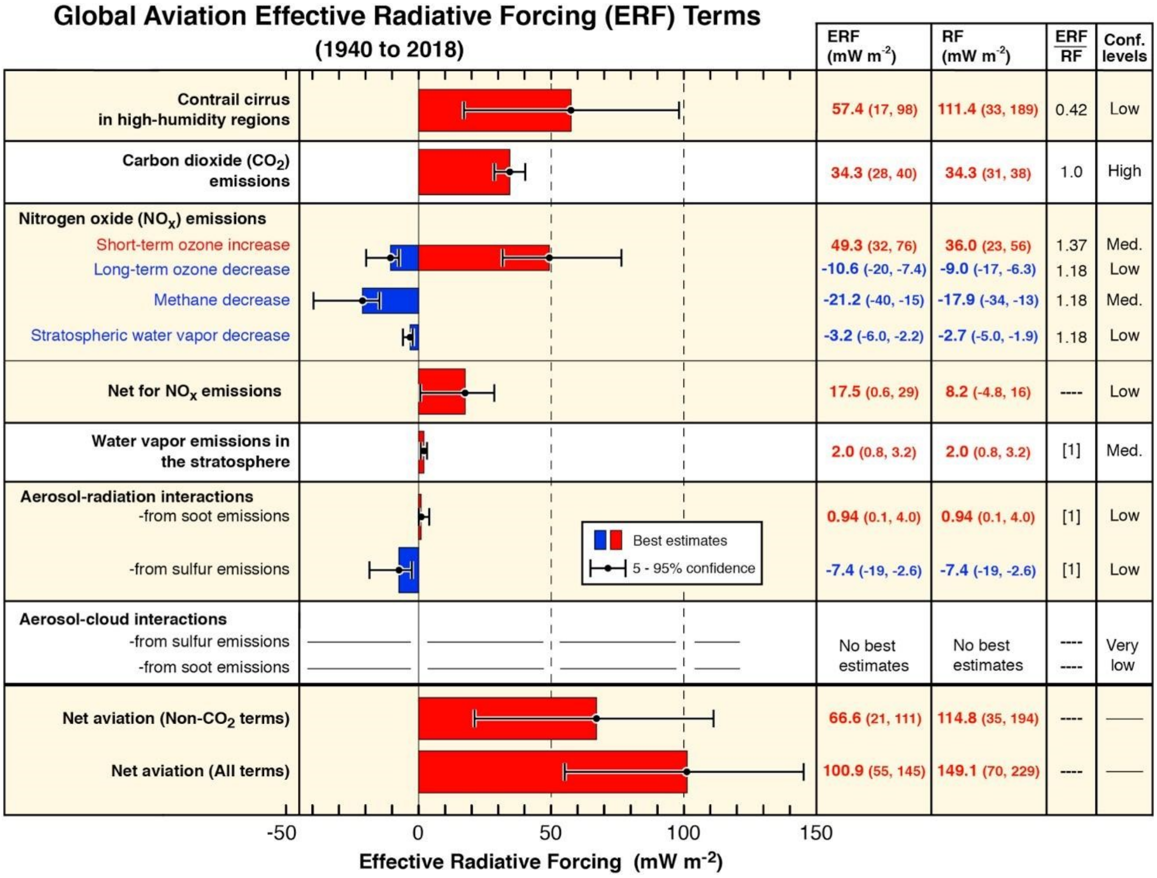

Figure 4.1. Best-estimates for climate forcing terms from global aviation from 1940 to 2018. The bars and whiskers show ERF best estimates and the 5–95% confidence intervals, respectively. Red bars indicate warming terms and blue bars indicate cooling terms. Numerical ERF and RF values are given in the columns with 5–95% confidence intervals along with ERF/RF ratios and confidence levels. RF values are multiplied by the respective ERF/RF ratio to yield ERF values. ERF/RF values designated as [1] indicate that no estimate is available yet and the arbitrary value of ERF/RF = 1 is used. From Lee et al., 2021, their Figure 3.

Different metrics are used to assess the climate impact of emissions. The Kyoto Protocol uses Global Warming Potential (GWP) with several time horizons as a metric. GWP is RF of a greenhouse gas normalised with RF from the same mass of CO_2, both accumulated over the time horizon in question. Given the complex relationship between radiative forcing and temperature for different radiative forcing compounds, GWP has occasionally been criticised, but the general acceptance and further development of the concept means that it is today widely used even for SLCP. To capture the impact of emissions on global mean temperature, the metric Global Temperature Potential (GTP) has been developed. This metric, in similarity with GWP, also uses different time horizons; the impact, however, shows the final impact at the end of the horizon. Even though the temperature response reflects a cumulative impact of RF over the time horizon, GWP and GTP for SLCP are very different. Both GWP and GTP can be expressed both as values relative to the corresponding mass emission of CO_2 or as absolute values in mW/m^2 and K, respectively. GTP can in some cases also address temperature response of the entire scenario instead of pulse emission of certain mass. Table 4.1 shows GWP and GTP on different time horizons and corresponding CO_2-equivalent emissions for the ERF components of 2018 aviation emissions and cloudiness, and in the bottom part also the CO_2-equivalent emissions based on these metrics.

Table 4.1. Emission metrics GWP and GTP with different time horizons Δt and corresponding CO_2-equivalent emissions for the ERF components of 2018 aviation emissions and cloudiness. E^*CO_2e arises from a simpler GWP method which defines the average annual rate of CO_2-warming-equivalent emissions (E^*CO_2e) over a period of Δt years arising from a particular component of ERF as a rate of CO_2 emission that would, alone, create the same rate of global temperature increase as the combined effect of aviation climate forcings (from Lee et al., 2021)

Metrics						
ERF term	GWP_{20}	GWP_{50}	GWP_{100}	GTP_{20}	GTP_{50}	GTP_{100}
CO_2	1	1	1	1	1	1
Contrail cirrus (Tg CO_2 basis)	2.32	1.09	0.63	0.67	0.11	0.09
Contrail cirrus (km basis)	39	18	11	11	1.8	1.5
Net NOx	619	205	114	-222	-69	13
Aerosol radiative forcing						
Soot emissions	4 288	2 018	1 166	1 245	195	161
SO_2 emissions	-832	-392	-226	-241	-38	-31
Water vapor emissions	0.22	0.1	0.06	0.07	0.01	0.008

CO_2-eq emissions (Tg CO_2 yr^{-1}) for 2018							
ERF term	GWP_{20}	GWP_{50}	GWP_{100}	GTP_{20}	GTP_{50}	GTP_{100}	GWP^*_{100} (E^*CO_2e)
CO_2	1 034	1 034	1 034	1 034	1 034	1 034	1 034
Contrail cirrus (Tg CO_2 basis)	2 399	1 129	652	695	109	90	1 834
Contrail cirrus (km basis)	2 395	1 127	651	694	109	90	1 834
Net NOx	887	293	163	-318	-99	19	339
Aerosol radiative forcing							
Soot emissions	40	19	11	12	2	2	20
SO_2 emissions	-310	-146	-84	-90	-14	-12	-158
Water vapour emissions	83	39	23	27	4	3	42
Total CO_2-eq (using km basis)	4 128	2 366	1 797	1 358	1 035	1 135	3 111
Total CO_2-eq/CO_2	4	2.3	1.7	1.3	1	1.1	3

Concept of RF of aviation emissions as instantaneous RF caused by historic emissions (from year 1940 onward) in a certain year has been introduced by the IPCC report 'Aviation and the Global Atmosphere' (IPCC, 1999). This concept is also used for the metric used by many climate calculators for air travel – the Radiative Forcing Index (RFI) – in which the RF from all aviation emissions is normalised with RF of aviation CO_2. RFI is a relevant metric that is separate from GWP; it is, however, often confused with GWP for aviation's SLCP. An important property of RFI is that the denominator, RF of CO_2, would change over time as the emitted CO_2 accumulates in the atmosphere even if emissions would keep constant. When used for assessment of concrete travel or flight, one also needs to be aware that RFI reflects the impact of the global aviation fleet and doesn't have a connection to the mass of SLCP on an individual level. Figure 4.2 shows ERF of different aviation forcing terms calculated by a climate model for the period 2000-2018 from Lee at al. (2021).

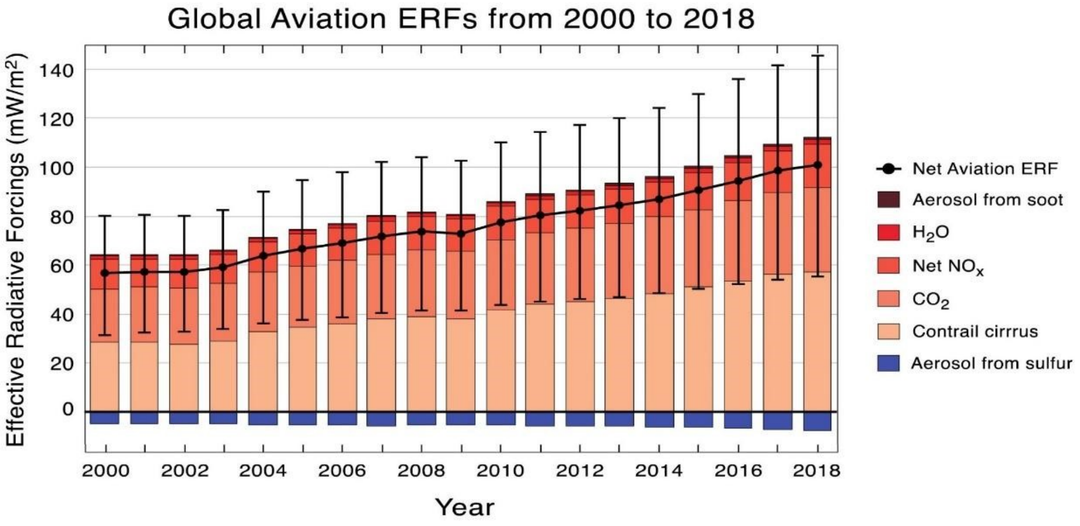

Figure 4.2. Time series of calculated ERF values and confidence intervals for annual aviation forcing terms from 2000 to 2018. The net values are not arithmetic sums of the annual values because the net ERF requires a Monte Carlo analysis that properly includes uncertainty distributions and correlations (from Lee et al, 2021, their Figure 6, upper panel).

4.2 Climate impact of contrails

Persistent contrails contribute substantially to the climate effect of aviation (Lee et al, 2009; Grewe et al., 2017; Lee et al, 2020). The annual and global mean radiative forcing (RF) of all contrails is of the order 50mW/m^2, which represents a third to one half of the total estimated RF of aviation. The instantaneous RF of a single contrail (iRF) can, however, be three orders of magnitude larger with both negative (cooling) and positive (warming) sign, and the estimates mentioned above is just the small net effect that remains when large negative and positive contributions almost balance with a small positive RF remaining (Gierens et al., 2020).

There are two conditions necessary for persistent contrails. First, the so-called Schmidt-Appleman criterion (Schumann, 1996) must be fulfilled so that the contrail formation is possible in a given situation. This criterion covers thermodynamic conditions in an early plume stage behind the aircraft and its fulfilment is given by a combination of atmospheric conditions and aircraft properties. The second condition required for persistent contrails is that the ambient air is in the state of supersaturation with respect to ice so that the contrail can persist and its ice crystals can grow by condensation.

To mitigate contrail-induced warming of the climate, it is not efficient to avoid all persistent contrails. Since only night-time contrails at specific conditions cause warming, the radiative forcing of the contrail during its lifetime needs to be calculated. Avoiding only those that produce individually the largest warming is sufficient to largely eliminate the overall climate effect of persistent contrails. For instance, Teoh et al. (2020) show on example of air-traffic data from Eastern Asia that selectively diverting 1.7% of the considered flights could lead to almost a 60% reduction of contrail EF, and the corresponding increase in fuel consumption and CO_2 emission would be 0.0014% for the considered fleet.

For the calculation of iRF Schumann et al. (2012) developed a parameterized analytical model to compute the IRF at the top of the atmosphere (TOA) produced by an additional thin contrail cirrus layer. The model calculates the iRF using as input the outgoing longwave radiation, and direct and reflected short-wave solar radiation values at TOA for a contrail-free atmosphere, so that the model is applicable for both cloud-free and cloudy ambient atmospheres. Additional input includes the contrail temperature, contrail optical depth at 550 nm, effective particle radius, particle habit, solar zenith angle, and the optical depth of cirrus above the contrail layer.

The required radiation quantities are included in the output of meteorological models also used for input of other meteorological data needed for calculation of Schmidt-Appleman criterion and ice-supersaturation, e.g., ECMWF or MEPS. The initial contrail properties depend on the aircraft while development of the contrail optical depth and its vertical and horizontal extension is driven by its mixing with humid ambient air. Contrails disappear when the bulk ice content is sublimating or precipitating.

Gierens et al. (2020) calculated IRF and contrails optical thickness with a simplified approach based on Schumann et al. (2012) using reanalysis 5 (ERA-5) data of the ECMWF (Hersbach et al., 2018) and compared these calculations with calculations based on humidity and temperature measurements of MOZAIC (Marenco et al., 1998). Figure 4.3a shows IRFs calculated with model and measured data, finding that cooling contrails (negative iRF) rarely occur, in less than 20% of cases, whiles large part of the cases shows zero and small positive iRF values and the most persistent contrails in the data have a slightly positive warming effect up to 10 W/m^2. Figure 4.3b shows comparison of contrail optical thickness based on these two datasets, optical thickness values are often larger than their reanalysis counterparts.

a)

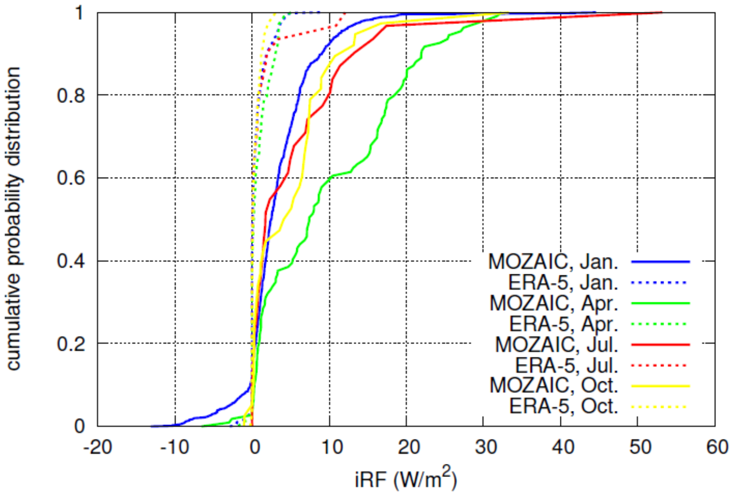

b)

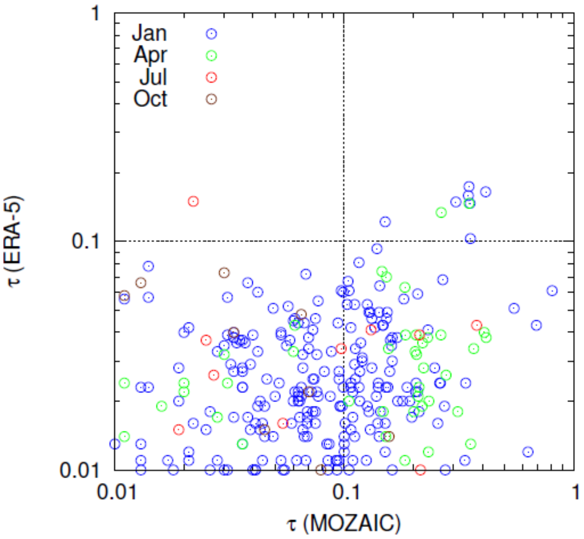

Figure 4.3. a) Cumulative probability distributions of instantaneous radiative forcing of contrails for January, April, July and October 2014 both for MOZAIC data (solid lines) and the corresponding times and grid points in ERA-5 (dashed). b) Scatterplot of optical thickness values for persistent contrails that occur in both MOZAIC (x-axis) and ERA-5 (y-axis). Colour coding as a) for the four months. From Gierens et al. (2020), their Figure 4.

4.3 Climatology of ice supersaturated and cloud free areas over Sweden and Europe

Climatologies of ice supersaturation can be constructed from both observations and models or combinations of the two. Observation types include in situ data from radiosondes or aircraft and remote sensing data from satellites. Björklund (2011) prepared a climatology of ice supersaturated layers, ISSL, over Sweden for the period 2006-2010 using radiosonde data from four locations, Visby, Landvetter, Sundsvall and Luleå. ISSL refers to atmospheric layers with ice supersaturation regardless of if they are simultaneously cloudy or not, while cloud free ice supersaturated layers are often termed ice supersaturated regions, ISSR. Figure 4.4a shows the monthly frequencies of ISSL as derived from the radiosonde data. As can be seen monthly average frequencies are in the range of 30-60% with a clear seasonal variation with higher values in winter. Figure 4.4b shows monthly average ISSL frequencies for the same four locations for the period 2007-2010 derived from the ERA Interim reanalysis (Dee et al. 2011) which is a combination of model simulation and observations providing in addition complete geographical coverage. The monthly average frequencies from radiosondes and the reanalysis are comparable although there are quite large differences (>20%) for individual months and locations.

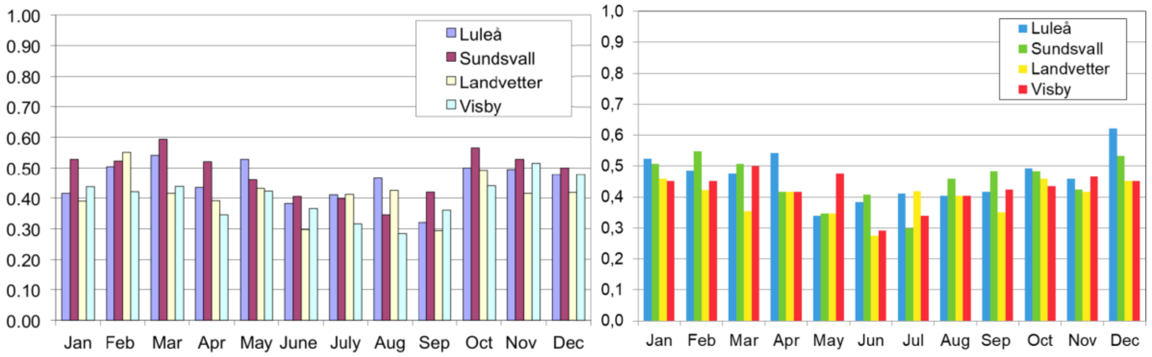

Figure 4.4. Monthly average frequencies of ISSL over Sweden derived from radiosondes (left panel) at 00 UTC for the period 2006-2010 (from Björklund (2011), their Figure 3) and from ERA Interim reanalysis data (right panel) at 00 UTC for the period 2007-2010.

Figure 4.5 shows the monthly average height of the ISSL at the four locations using the same data. Here we also see a clear seasonal variation with ISSL occurring at higher levels in summer than in winter. We can also see that ISSL on average occurs in the upper part of the troposphere above 400 hPa according to the observations. The reanalysis data gives similar heights as observed in summer but are biased towards higher levels (lower pressure) by about 50 hPa in winter.

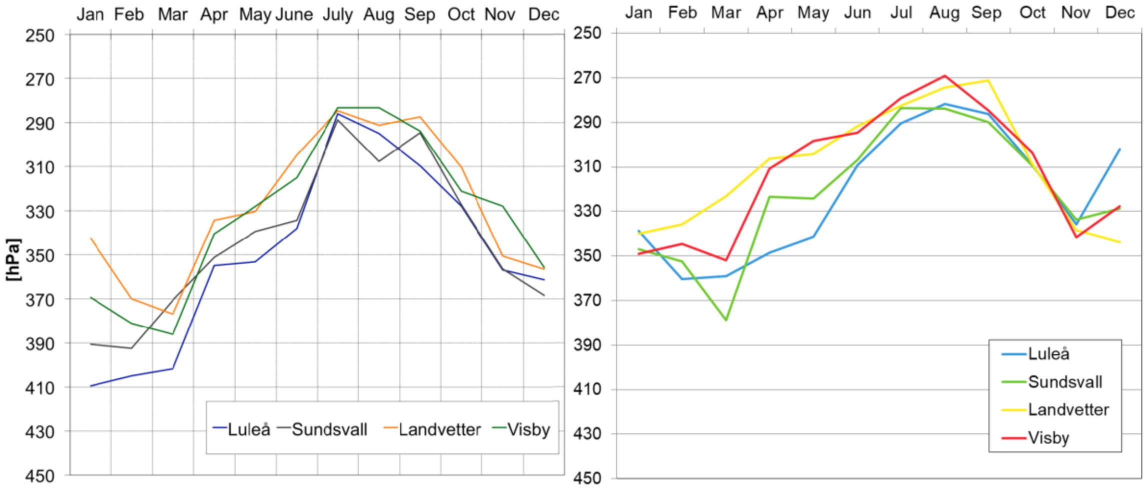

Figure 4.5. Monthly average height of ISSL over Sweden derived from radiosondes (left panel) at 00 UTC for the period 2006-2010 (from Björklund (2011), their Figure 4) and from ERA Interim reanalysis data (right panel) at 00 UTC for the period 2007-2010.

Petzold et al. (2020) presented an analysis of the occurrence of ice supersaturation in the northern hemisphere mid latitudes between North America and Europe based on in-situ measurements onboard commercial aircraft. Figure 4.6 shows the seasonal cycle of ice supersaturation over Europe from their analysis. Average frequencies are quite comparable to those presented in Figure 4.4 for Sweden and also the seasonal variability is in the same direction with lower frequencies in the summer than in other seasons. Note that although the label on the vertical axis in Figure 4.6 is ISSR the information given is actually corresponding to ice supersaturated layers, ISSL.

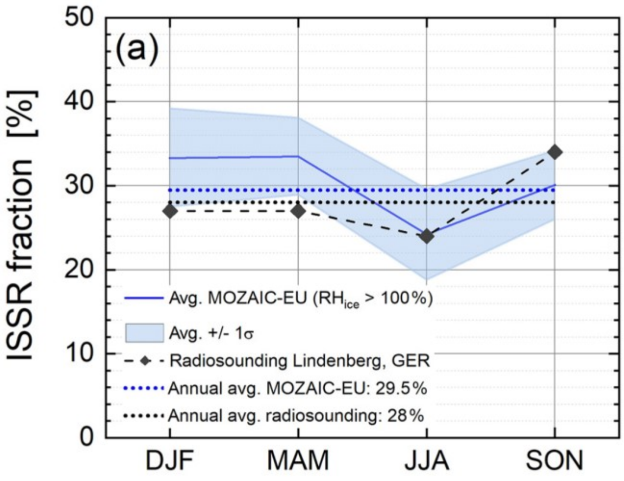

Figure 4.6. Seasonal average fraction of ice supersaturation as observed from commercial aircraft over Europe for the period 1995-2010 in the layer 0-60 hPa below the thermal tropopause (from Petzold et al., 2020, their Figure 13a). Also shown is frequency of ice supersaturation as observed by radiosondes at Lindenberg in Germany for the same time period.

Data from numerical weather prediction (NWP) systems has the advantage of providing spatial coverage of meteorological variables. As an example, Figure 4.7 shows annual average frequency, height and thickness of ISSL and ISSR over Europe at 00 UTC derived from operational European Centre for Medium-Range Weather Forecasts (ECMWF) predictions for 2007. For ISSR a threshold of 33% cloud cover was used, i.e., if the cloud cover at the level where ice supersaturation occurs is greater than 33% then that level is not considered as an ice supersaturated region. The model data indicates that average frequencies of both ISSL and ISSR increase with latitude and that average height decreases (increasing pressure) with latitude. The latter is natural as the tropopause height decreases going north. According to the model data also the depth of supersaturated layers increases with latitude. The frequency of ISSR is about 10% lower than for ISSL, while the average height is higher (lower pressure) and the thickness is lower for ISSR in the model data.

In summary, observations and model data for ice supersaturation over Europe are broadly consistent indicating a frequency of ice supersaturated layers (ISSL) of 30-60% over Scandinavia. When accounting for co-occurrence of cloudiness using model data the frequency and thickness of ice supersaturated layers is reduced and the average height increases (pressure decreases).

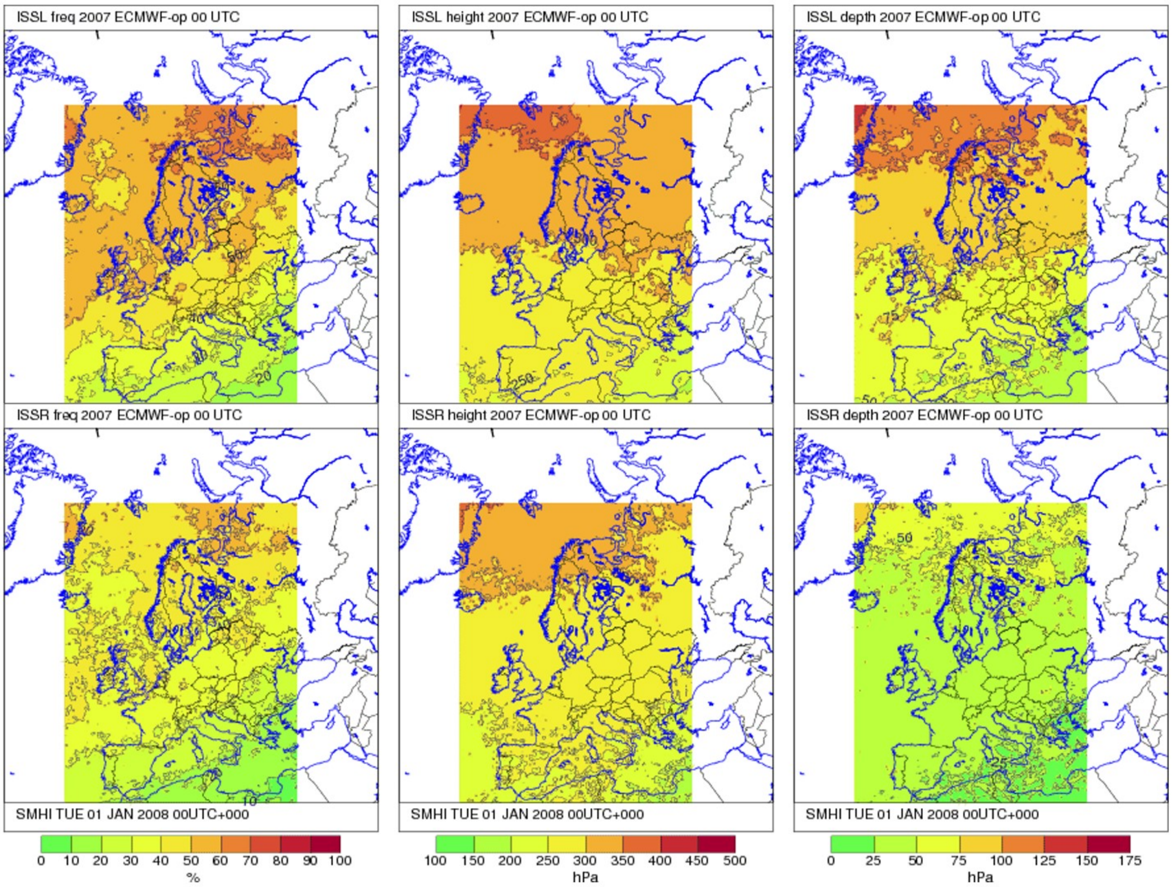

Figure 4.7. Annual average for 2007 frequency, height, and thickness of ISSL (top row) and ISSR (bottom row) over Europe at 00 UTC derived from operational ECMWF forecasts.

4.4 Performance of operational NWP models for ice supersaturation

When considering the possibility of diverting air traffic to avoid regions where persistent contrails may form, the quality of NWP forecast data becomes important. In this project two main sources of

NWP data have been used; ECMWF with their global operational model IFS (Integrated Forecasting System) and MetCoOP with their high-resolution regional model AROME. MetCoOp is an operational collaboration for NWP between Sweden, Norway, Finland and Estonia. In the first phase of the project efforts were spent on validating the models with regard to ice saturation. Figure 4.8 shows a comparison between model simulated and observed relative humidity over ice at the 300 hPa level for the period February-April 2020. Observations are from 28 radiosonde stations in north-western Europe and model data are from 36- and 48-hour forecasts. The observed ambient temperature for these cases were between -40 and -65 deg C. As can be seen both the ECMWF model and AROME tend to underestimate relative humidity over ice close to or above 100%. Up to 50% supersaturation is seen in the observations while the models only in a few cases reach 30% and mostly are below 20% supersaturation, The ECMWF model has a smaller spread and error compared to AROME, while AROME has some more events of supersaturation.

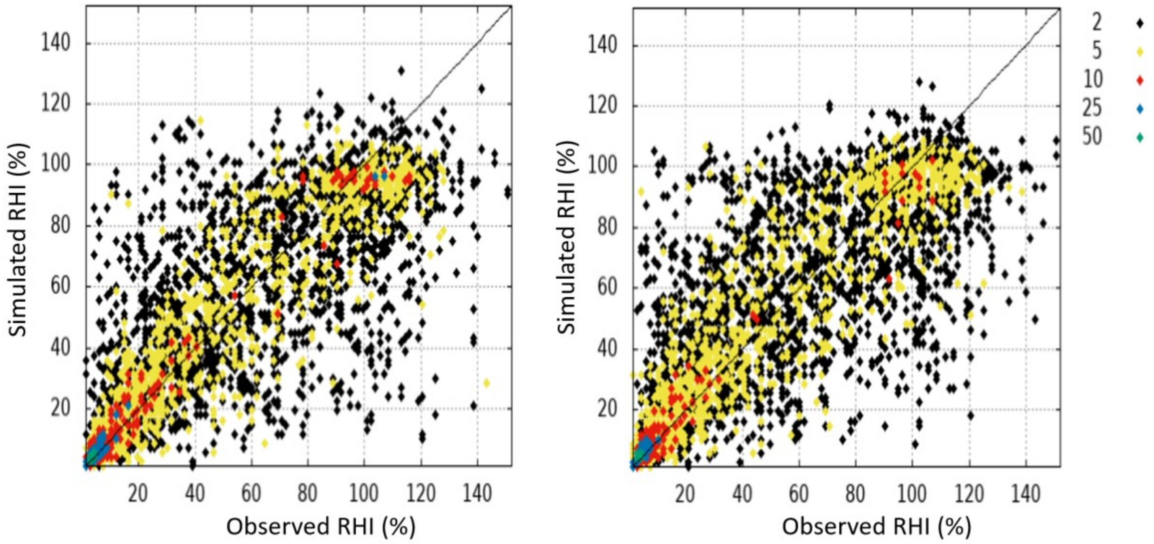

Figure 4.8. Comparison between observed, radiosondes, and forecast relative humidity over ice (RHI) for 28 stations in north-western Europe for the period February-April 2020 from the ECMWF operational model (left) and from the MetCoOp operational model, AROME, (right). 36- and 48-hour forecasts. Units: Relative humidity over ice (%).

The validation reveals that the occurrences of supersaturation with respect to ice are under-forecast near the tropopause, where most of the aviation takes place. Reducing the number concentration of cloud ice water crystals in the model is one way to slow down the deposition of ice and thus prolonging a supersaturated environment. The number concentrations used in the present version of the AROME model is based on the work by Meyers et al (1992). It originates from measurements between -10 C and -30 C but is used also for the colder temperatures commonly present near the tropopause, thus less valid in this region. The prescribed number concentration is approximately tenfold for every drop of the temperature of 10 degrees. The test presented here is just to limit the number concentration to what is used at 238 K (about -35 C).

Figure 4.9 shows a comparison between the validation of the operational model and the modified model for a 19-day period in June 2020. The result is some improvement of the forecast of relative humidity with respect to ice, but there is still some underprediction. The remaining under-prediction may partly be caused by poor vertical resolution. The validation result for other variables is mainly neutral for the same time period. A winter period has also been tested with a similar result (not shown). An alternative to an upper limit of the ice number concentration, is to assume a less steep increase with decreasing temperature e.g., below -30 C. This has not been tested yet.

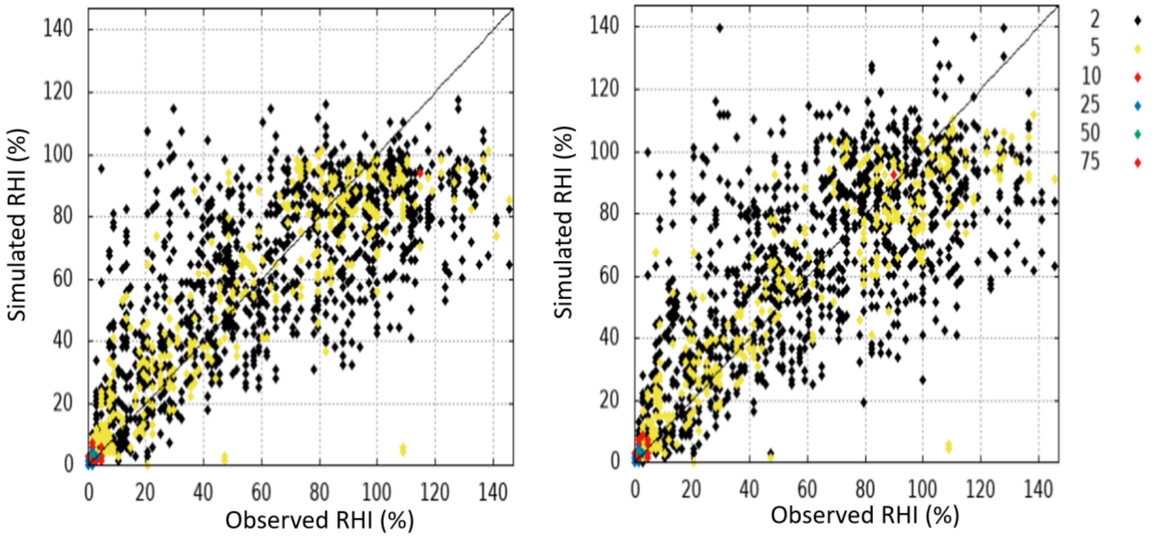

Figure 4.9. Forecast, 12, 24, 36 and 48 h, relative humidity over ice (vertical axis) compared to observations in north-western Europe for 19 days in June 2020 (horizontal axis) for soundings at 250 hPa. Reference experiment to the left and the test to the right. Units: Relative humidity over ice (%).

4.5 Comparison of ice supersaturation forecasts with visual observations of contrails

When the Covid-19 pandemic arrived in 2020 commercial air traffic almost stopped. The effect was dramatic in terms of reduction of noise and visual signs in the sky from air traffic. This also meant that it was quite easy to make observations of contrails and to link them to individual aircraft. To take advantage of this special situation a simple observation protocol for contrails was set up and observers were recruited among people doing climate observations across Sweden on behalf of SMHI. The climate observers were asked to report observations of contrails, including time, location, cloud cover, and if the contrail was persistent or not. Optionally they could also report the height of the aircraft using information from e.g., FlightRadar24. Using a database of all aircraft movements over Sweden available at LFV, missing reports of aircraft height could later on be added to the manual observations. In total 38 climate observers reported 267 observations of contrails/no contrails during the period May-August 2020. 200 of these observations indicated persistent contrails while the remaining indicated short contrails or contrails that rapidly dissolved.

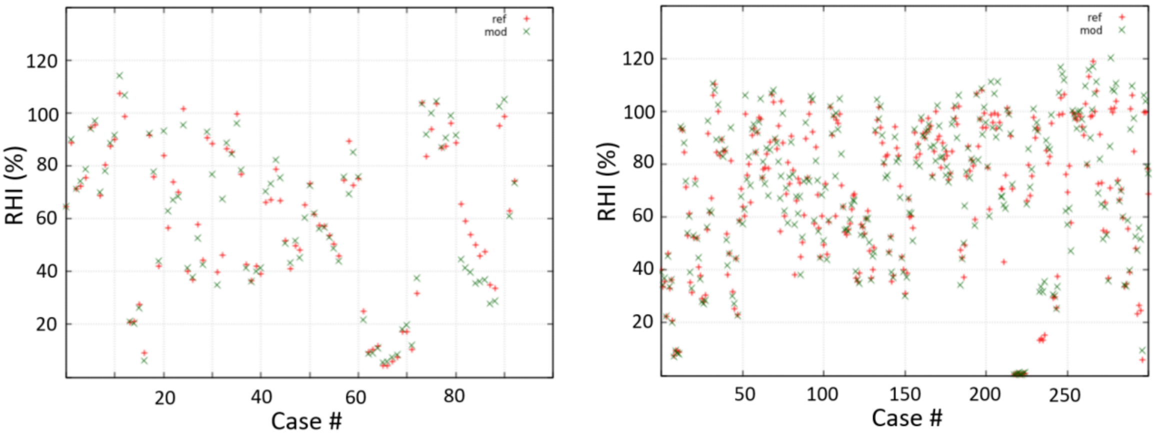

Figure 4.10. Forecast relative humidity over ice on the vertical axis using reference (red crosses) and modified version (green cross) of the AROME forecast model for observations of contrails during the time periods 1-19 June and 2-28 July 2020. The horizontal axis indicates the time sequence of the observations. Note that in order to increase the statistical sample 3 or 4 different forecast lengths were compared to each observation. Units: Relative humidity over ice (%).

Forecasts of relative humidity over ice corresponding to the observations of aircraft contrails were extracted from model runs using the standard and modified versions of the AROME described in section 4.4. The results are displayed graphically in Figure 4.10 and summarised in Table 4.2. As can be seen, the forecast of RHI is higher when persistent contrails are observed, average 73-75% compared to 52% when no persistent contrails are observed with the modified version of the model giving the slightly higher value. Also, the fraction of cases higher than a threshold of 100, 90, 80 or 70% RHI is about twice as high for the cases with observed contrails compared to the cases without contrails. However, the fraction of cases with forecast RHI above 100% is quite low, 8-18%, for observations of persistent contrails and even the fraction above 90% is only 35-38% for the standard and modified model version respectively. This points in the same direction as the comparison to radiosonde data presented in Section 4.4, that the forecast models underestimate relative humidity over ice, at least in the upper range of relative humidity. On the other hand, it should be noted that persistent contrails are observed also when the forecast RHI is below 70%. This could be due to that "persistence" was not clearly enough defined for the observers or sometimes difficult to observe.

Table 4.2. Statistics of forecast ice supersaturation, RHI, with reference version of the AROME forecast model and the modified version of the model as described in section 4.4. In order to increase the statistical sample 3 or 4 different forecast lengths were compared to each observation.

RHI (%)	REF no contrail cases (%)	MOD no contrail cases (%)	REF contrail cases (%)	MOD contrail cases (%)
>100	3	3	8	18
>90	15	14	35	38
>80	27	28	55	54
>70	38	38	64	65
Mean RHI (%)	52	52	73	75
Total # cases	143	143	370	370

4.6 Calculation of energy forcing of contrails

4.6.1 Methodology

In OP-FLYKLIM we have developed a method for calculation of energy forcing of individual contrails that can be formed by an aircraft along its route. As the method is aiming to climate optimisation of the flight routes, the atmosphere along the planned flight route is first tested for relative humidity supersaturation with respect to ice and for the Schmidt-Appleman criterion (Schumann, 1996) using temperature and humidity fields from MetCoOP and their ensemble prediction system MEPS, for Northern Europe weather prediction. The model grid cells fulfilling both conditions are clustered into ISSL polygons stretching over areas at different flight-level intervals.

For each ISSL polygon a number of randomly selected 'seeds' is chosen, the number being proportional to the polygon area. These seeds, representing unit length of the flight, are initiated with contrail formed from exhaust of a defined aircraft under conditions of the actual flight phase. Mass of the exhaust gases m_e is calculated from the fuel consumption FC (in kg/s), obtained by the FOI-3 method described in Chapter 3, and aircraft speed v_a (in m/s), mass of emitted water vapour m_{H2O} (in g) then with help of its emission factor EF_{H2O} (use 1240 g/kg fuel):

$$m_e = FC / v_a \qquad \text{(E1)}$$

$$m_{H2O} = EF_{H2O} * m_e \qquad \text{(E2)}$$

Each seed is then followed by the model forward in time and space using 3-dimensional wind fields of the MEPS forecast on 20-min temporal resolution. Evolvement of the seed-contrail properties including its horizontal and vertical extension, optical depth and iRF is calculated using methods described in Schumann et al. (2012a and 2012b), the gaussian dispersion of the contrail in Konopka et al. (1995) and temperature, humidity and TOA radiation fields of the MEPS forecast. As long as the seed is dispersing into an ice-supersaturated environment, its ice particles grow by condensation. When humidity in the seed becomes undersaturated with respect to ice, the ice particles sublimate and the seed is terminated. Examples of the ISSL polygons with seeds and their fate in the atmosphere calculated along the routes ARN-KRN and HEL-AMS for days with high persistent-contrail-formation potential is shown in Figure 4.11

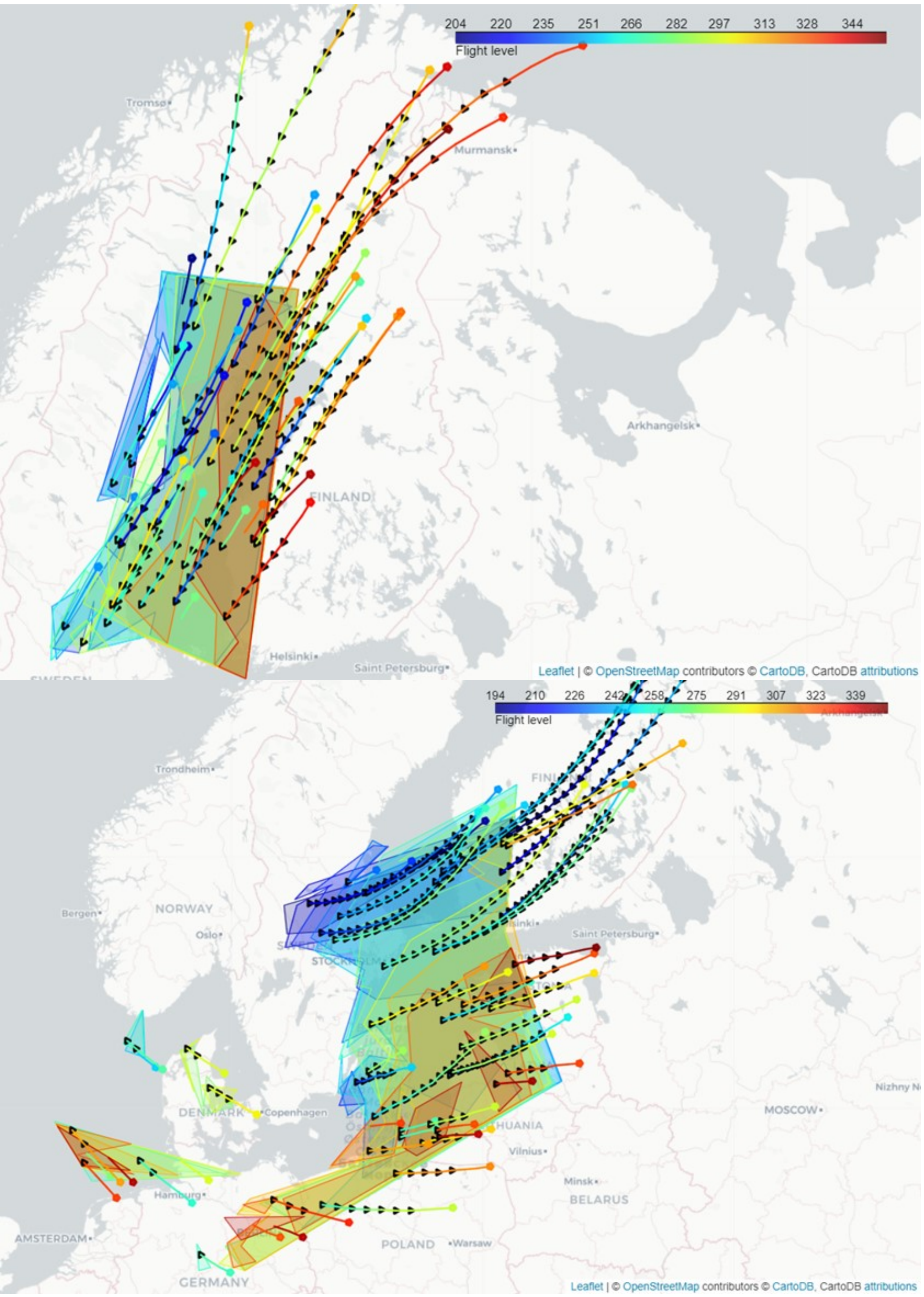

Figure 4.11. ISSL Polygons with seeds and their fate in the atmosphere calculated along the route ARN-KRN 2022-02-03 (upper panel) and HEL-AMS 2022-04-03 (lower panel). The black triangles show 3-d transport of the seed in an ice-supersaturated atmosphere in 20-min intervals until their endpoint (hexagon) where the atmosphere is not ice-supersaturated. Colour coding shows altitude as flight level (in hundreds of feet), both for ISSL polygons, seed transport trajectories and the end-point hexagons.

The initial dispersion of the plume and development of the contrail ice is calculated according to Schumann et al. (2012b): The aircraft engine exhaust initially sinks and under time t_0 dependent of the aircraft wingspan, mass and its true velocity through the air keeps in expanding coherent vortex in so-called vortex regime. The dispersion Nd_{vor} (dimensionless) during this phase is parameterised as:

$$Nd_{vor}(t_0) = 7000 * t_0^{0.8} \qquad (E3)$$

After time t_0 the vortex dissipates and the contrail disperses in a gaussian regime with $Nd_{gaus}(t)$. The volume of the plume segment at time t is defined by the volume occupied by the exhaust gas under the pressure and temperature conditions of the surrounding atmosphere and the dispersion at t. As the condition of the seed is that it initially fulfils the Appleman criterion and is dispersing into ice-supersaturated background air during its existence, its ice water content is equal to the integral of water vapour concentration above the ice supersaturation contained in the background air that is mixing into the seed plus the water vapour emitted from the aircraft, the latter being in most cases only a very small contribution. The ice water content and vertical extension of the contrail is used to calculate its optical depth τ and iRF.

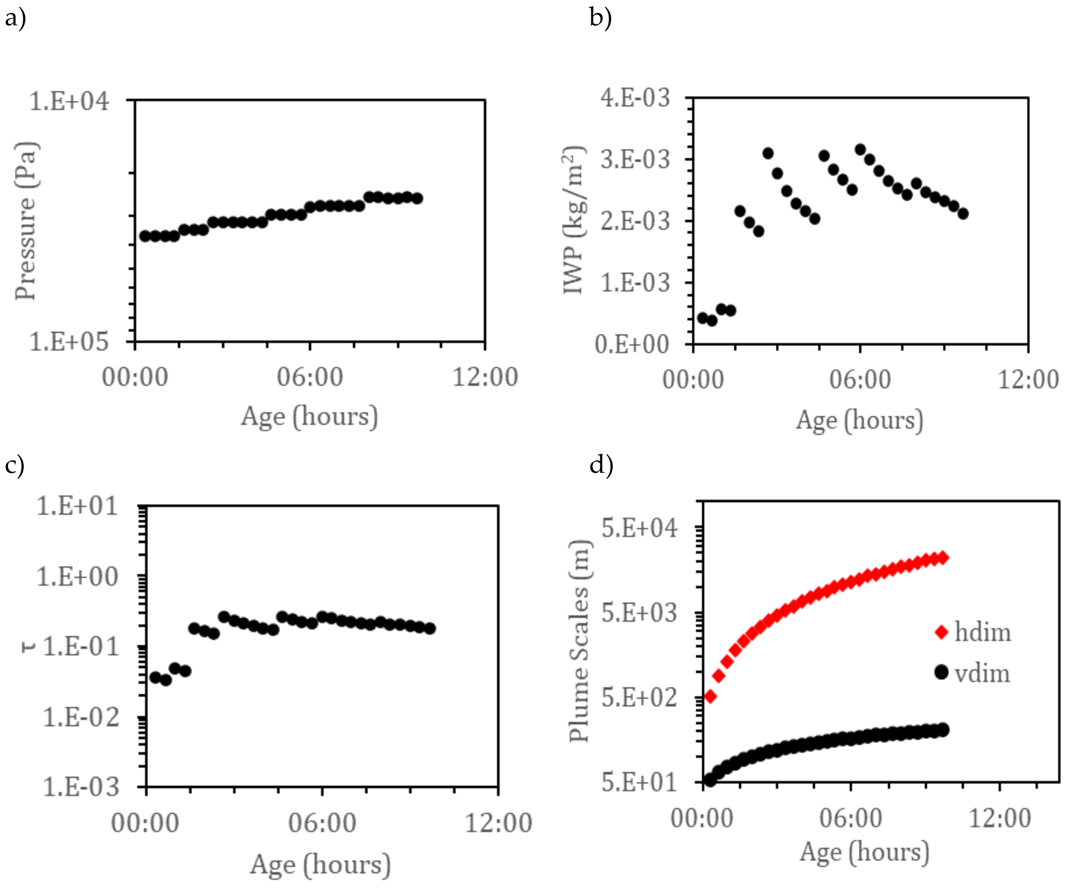

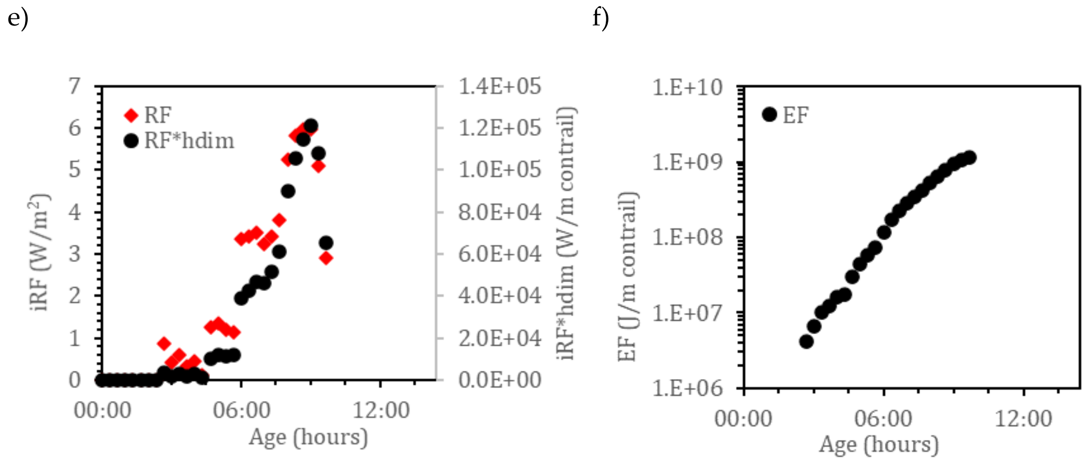

Figure 4.12. Example of development of pressure (a), ice water path IWP (b), optical depth (τ) (c), plume scales width (hdim) and depth (vdim) (d), iRF (f) and accumulated energy forcing EF (g) in a simulated contrail.

The product of iRF calculated at each time-step iRF_{t_x} and the actual width of the contrail w_{co_x}, integrated over the lifetime of the contrail gives energy forcing of a unit length of the flight EF_{com_x} (in J/m flight) at the place of the seed. In the model this is calculated as:

$$EF_{com\_x} = \sum_{x=1}^{x_{end}} iRF_{t\_x} \times w_{co\_x} \times \Delta t \tag{E4}$$

Mean EF_{com_x} values of all seeds in each ISSL polygon are assumed to be the EF_{com_x} of that polygon. From l_{co_p}, distances flown through each polygon, we get the EF of each part of the route flown through the ISSL polygon, EF_{co_p}, and of the entire route, EF_{co_r} (in J).

$$EF_{co\_p} = EF_{com} \times l_{co\_p} \tag{E5}$$

$$EF_{co\_r} = \sum_{x=1}^{n} EF_{co\_px} = \sum_{x\_1}^{n} EF_{co\_px} \times l_{co\_px} \tag{E6}$$

Where x are all ISSL polygons crossed by the flight route.

The EF_{co_r} can be related to EF from a mass of CO_2 on certain time horizon *th* emitted on the flight if we know EF of unit mass of CO_2 on this horizon (EF_{CO2} in J/m² or EF_{totCO2} in J) where EF_{CO2} is the same as $AGWP_{CO2}$ available e.g. in the IPCC AR5 report (IPCC, 2014) and EF_{totCO2} is EF_{CO2} multiplied by the earth's surface S_{Ea}:

$$EF_{totCO_2} = EF_{CO_2} \times S_{Ea} \tag{E7}$$

According to IPCC (2014) EF_{CO2} is 2.5E-14 and 9.2E-14 W/m²/yr/kg on a 20 and 100-years horizon, respectively, which corresponds to EF_{totCO2} of 12.7 and 46.8 W/yr/kg. Assuming emission factor 3.16 kg CO_2/kg jet fuel and fuel consumption of 0.0025 kg fuel/m flight, these EF_{CO2} give energy forcing of CO_2 from 1m of flight on a 20 and 100-years horizon 3.16E+6 and 1.17E+7, respectively.

4.6.2. Results

During three months in 2022 (February, March , April) SMHI analysed meteorological fields of their operational forecast model for areas with potential for formation of persistent contrails fulfilling both the ice-supersaturation and Appleman criterion along two flight routes, Stockholm, Arlanda (ARN) - Kiruna (KRN) and Helsinki, Vantaa (HEL) - Amsterdam, Schiphol (AMS) for evening flights starting at 18:00 UTC. These ISSL polygons were then analysed at IVL for energy forcing (per m flight EF_{com_x}) of the potential contrails using the above-described methodology and operational weather-forecast model data downloaded from MEPS database. In the next step the energy forcing of flights between these two airport pairs, both in each polygon crossed and on the whole flight, were calculated by multiplying the EF_{com_x} by distance of the flight flown through each ISSL polygon. During this three-months period (89 days) for 60% - 65% of the evening flights some polygon with potential of formation of contrails with positive energy forcing occurred in the area, however, only a small part of the identified ISSL polygons were in the way for the flight. This section provides analysis of the ISSL polygons properties while their impact of radiative forcing from the flights is presented in Chapter 5.

Figure 4.13 provides characteristics of the identified ISSL polygons in terms of number of ISSL polygons in each flight route area, their total area, distribution over flight layers as well as mean and maximum lifetime and potential EF per m flight of the ISSL polygons for each flight. Scatter plot of ISSL polygons energy forcing EF_{com} against their lifetime (Figure 4.14) shows that the lifetime is an important parameter affecting the contrail energy forcing. In Figure 4.15 we relate their climate-forcing potential expressed as equivalent to CO_2 emitted from kg of jet fuel (estimated through combining the EF_{com} with polygons' horizontal extension estimated as the square root of their area) to the lifetime for different flight-level intervals. The figure shows correlation even if the scatter is high. For the studies period ISSL polygons with long lifetimes and hence eEFs are in the lower flight-level intervals.

a)

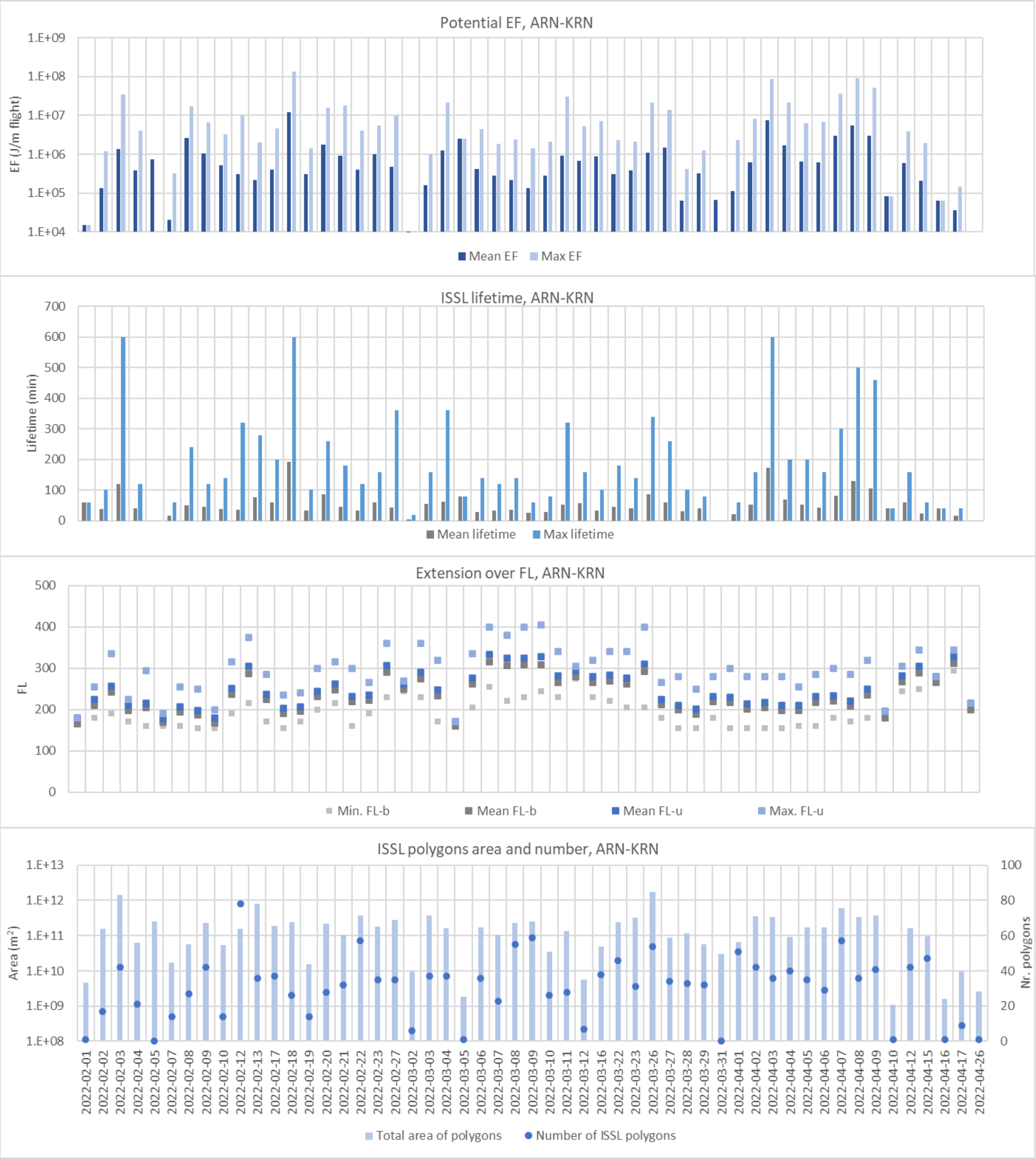

Figure 4.13. Continues

b)

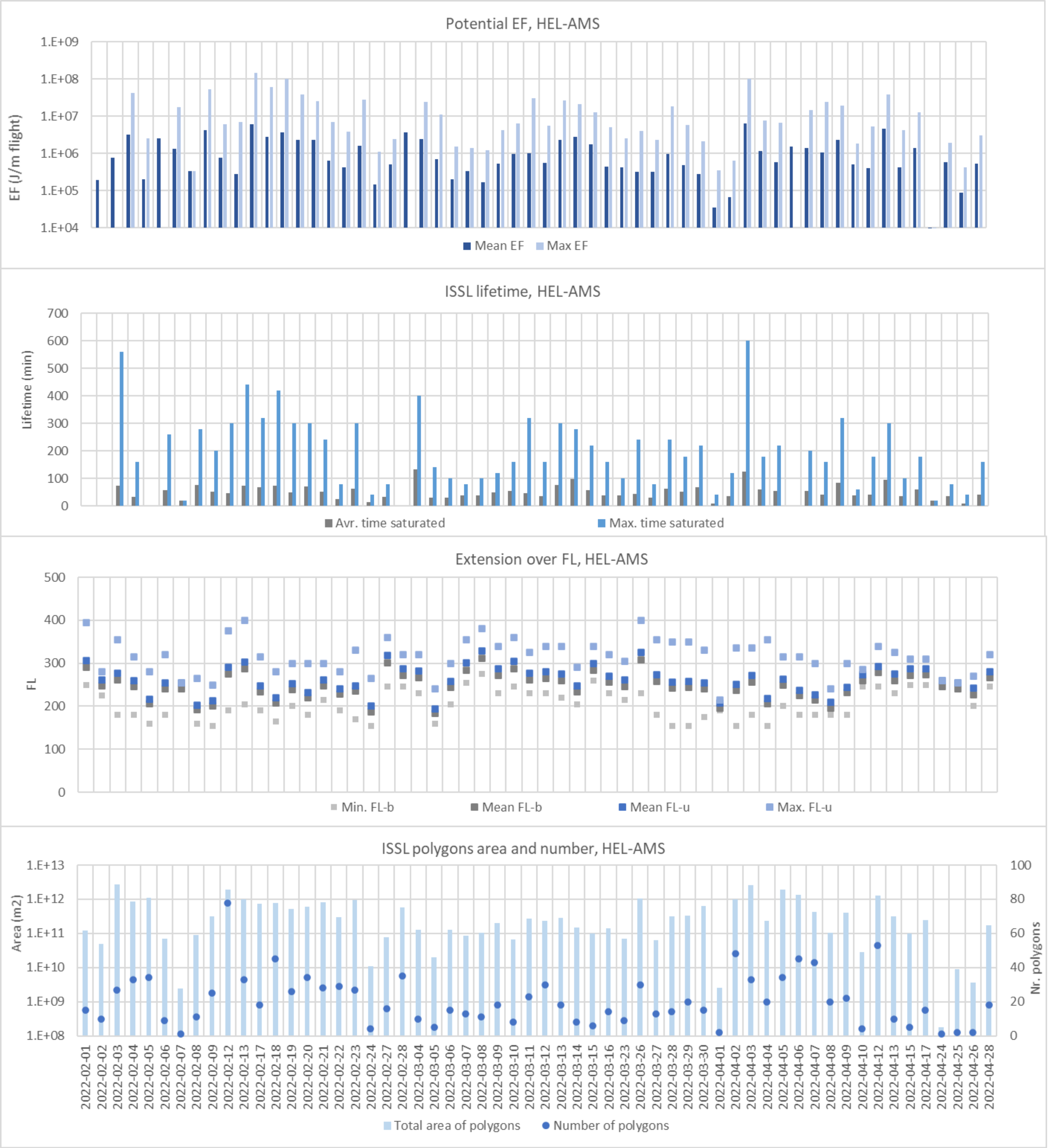

Figure 4.13. Characterisation of the ISSL polygons identified in a wider area of flights between ARN-KRN (a) and HEL-AMS (b) at 18:00 during the studied 3-months period. Mean and maximum potential energy forcing EF$_{tot\_x}$ (J/m flight) of ISSL polygons for each day, ISSL polygons mean and maximum lifetime, extension over the flight levels (FL in hundreds of feet), total area (m²) and number

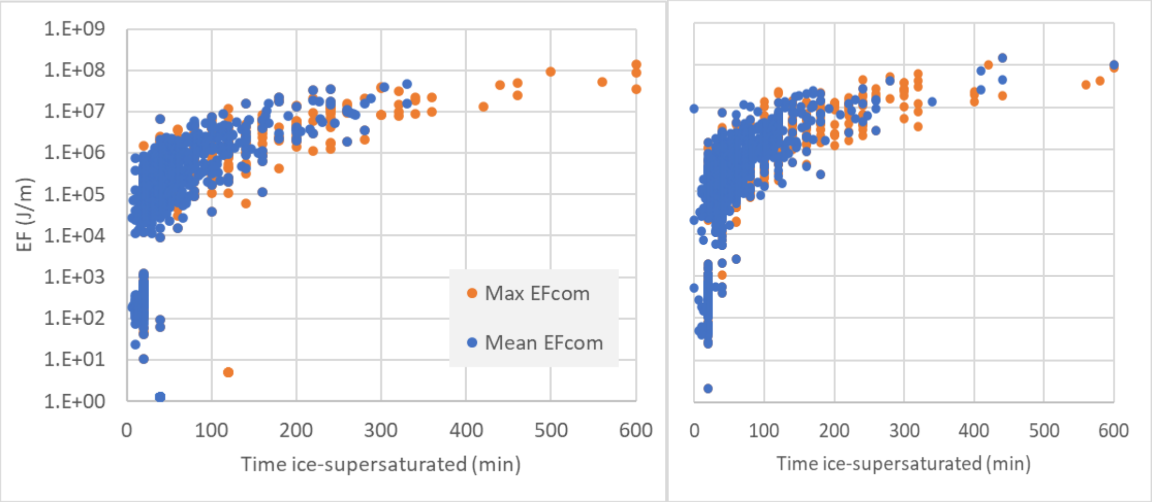

Figure 4.14. Scatter plot of ISSL polygons' energy forcing EF_{com} against their lifetime along the route ARN-KRN (left) and HEL-AMS (right).

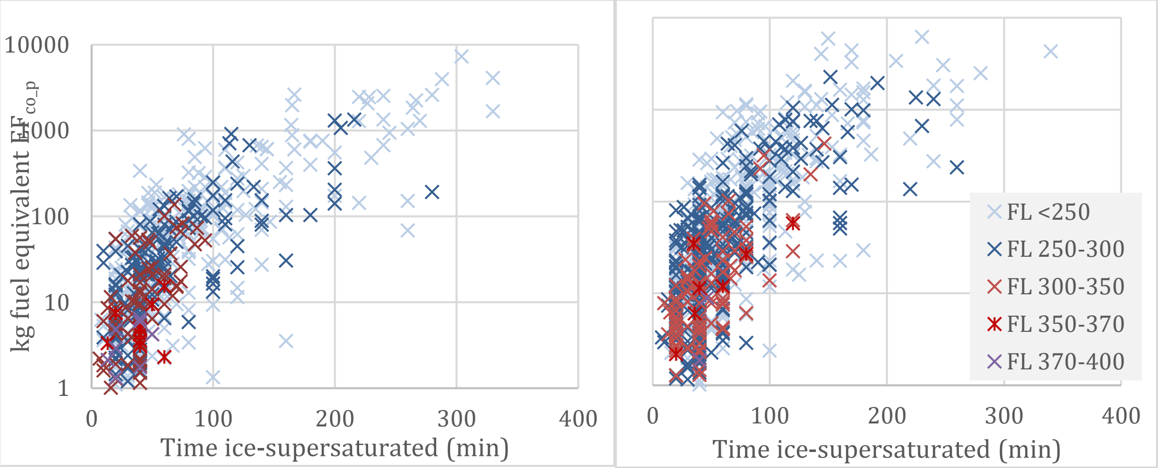

Figure 4.15. Climate-forcing potential of the investigated ISSL polygons along the route ARN-KRN (left) and HEL-AMS (right), expressed as EF_{co_p} in equivalent CO_2 emitted from kg of jet fuel on a 20-years horizon, plotted against their mean lifetime. The horizontal extension of the polygon is reflected as potential distance flown in the polygon equal to the square root of its area. Colour shows the flight-level interval of the initial position of the ISSL polygon.

5 Operative route optimisation for minimising the climate impact

(Output of AP5; Authors: Joakim Langner, Jana Moldanova, Michael Priestley, Ulrika Ziverts, Jens Wilhelmsson, Henrik Ekstrand)

5.1 Background

One of the goals of the project was to demonstrate the use of route optimization to reduce climate impacts. It was decided to approach this goal in a stepwise manner by starting to test procedures for route optimization early on in the project together with the airline companies involved. The plan was then to update these procedures when updated methods for estimating climate impacts had been developed in the project.

5.2 Methodology

5.2.1 Alternative routes for ARN-KRN in spring 2020

The first set of route optimizations was carried out in collaboration between SMHI and Novair for the ARN-KRN route. This route was chosen because it is sufficiently long to allow the aircraft to reach the higher flight levels usually used on longer routes and therefore also the possibility for high-altitude climate effects. For this set of route optimization the only criteria was to avoid ice supersaturated regions along the route, thereby focusing on avoiding creation of persistent contrails. Other climate effects were not considered when constructing alternative routes. In order to simplify the procedures involved, the Schmidt-Appleman criterion was also not considered in this first set of route optimizations.

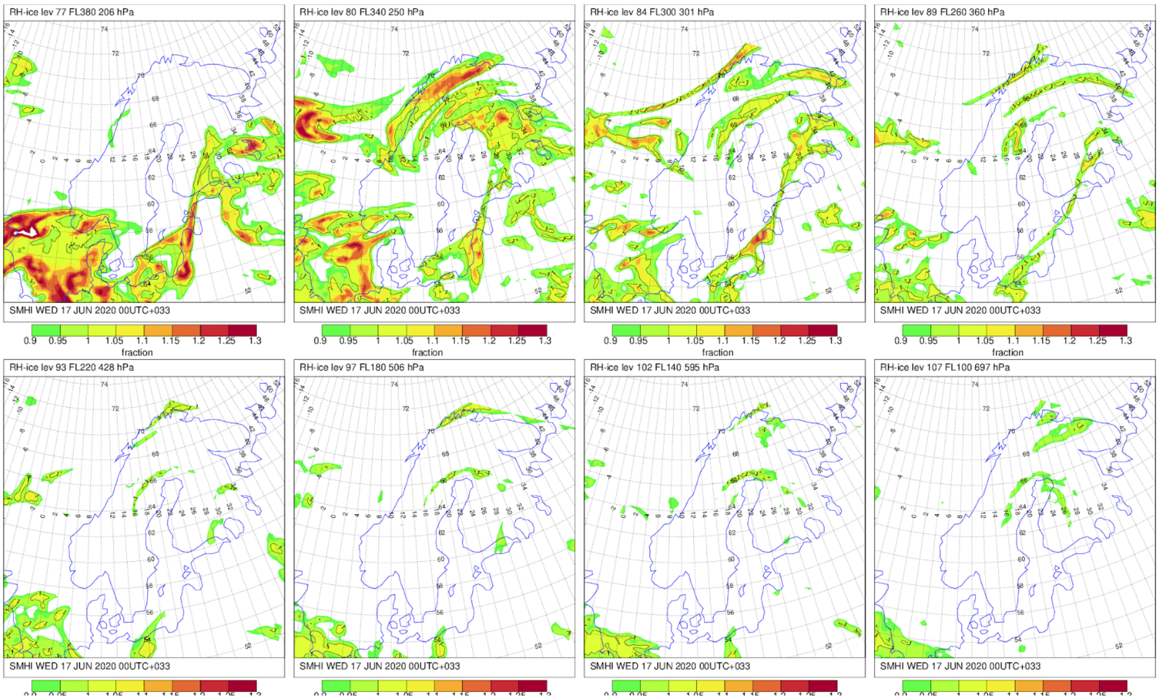

Figure 5.1. 33-hour forecast of relative humidity with respect to ice (fraction) over northern Europe for different flight/pressure levels valid at 09 UTC 2020-06-18.

As an example of meteorological information used in the route optimization Figure 5.1 shows the relative humidity with respect to ice as forecast by ECMWF over northern Europe at 09 UTC on the 18th of June 2020. For this case, ice supersaturation was forecast along the northern part of the route ARN-KRN. This information was used by SMHI to manually specify deviations from a standard direct route, see Figure 5.2, in order to avoid ice saturated areas. In this example the ice deviation route was to reduce height to flight level 240 (7200 m) from latitude 64 deg. N and to the end of the route in KRN. The alternative route was sent in text format via email to Novair as shown to the left in Figure 5.2.

Ice deviation route for ARN – KRN
2020-06-18 08:00 UTC

RESNA -
OSK –
RASEN -
64000N019008E FL<240
REKMI FL<240
OSKIR FL<240
ITVAV FL<240
VAGAS FL<240

Nominal route

Figure 5.2. Example of ice deviation route for ARN-KRN on the 18 June 2020 08 UTC (left). The waypoints RESNA in the south and VAGAS to the north are the first and last waypoints after leaving ARN and approaching KRN respectively. In between lies four waypoints for the nominal route (right).

In order to simulate operational procedures, the alternative route was sent on the day before the actual flight time or in the morning the same day, in the case of an evening flight, in order to allow Novair to do the route planning well in advance of the actual flight time. This meant that forecast lead times used were in the order of 30 hours. In an operational setting lead times could be reduced. Novair used their operational route planning tool to prepare four different flight plans:

1. Nominal route. Fixed route as in Figure 5.3 taking actual wind forecast into account.
2. Nominal route without taking the wind forecast into account (‘zero wind’ route).
3. Route following deviations suggested by SMHI to avoid ice supersaturated regions.
4. Same as 3 but without taking the actual wind forecast into account.

In the period April-June 2020 the presence of ice supersaturated regions along the route ARN-KRN was investigated on 60 occasions. These included both flights ARN-KRN in the morning and KRN-ARN in the evening. On 42 (60%) of the occasions regions of ice supersaturation was forecast along the route. For these 42 occasions Novair prepared flight plans for the four different cases listed above. Deviations suggested by SMHI could be either changes of flight level or change of route in the horizontal or a combination of these. From the flight plans the predicted fuel consumption was extracted and compared. Figure 5.3 summarises the results. The type of aircraft assumed in the optimization was an Airbus A321neo which is the type of aircraft Novair used in their operations. Increase in fuel consumption for ice deviation routes varies between close to zero and about 15%. The average increase in fuel consumption was 6.5% when accounting for forecast winds and 6.6% when winds were set to zero in the optimization.

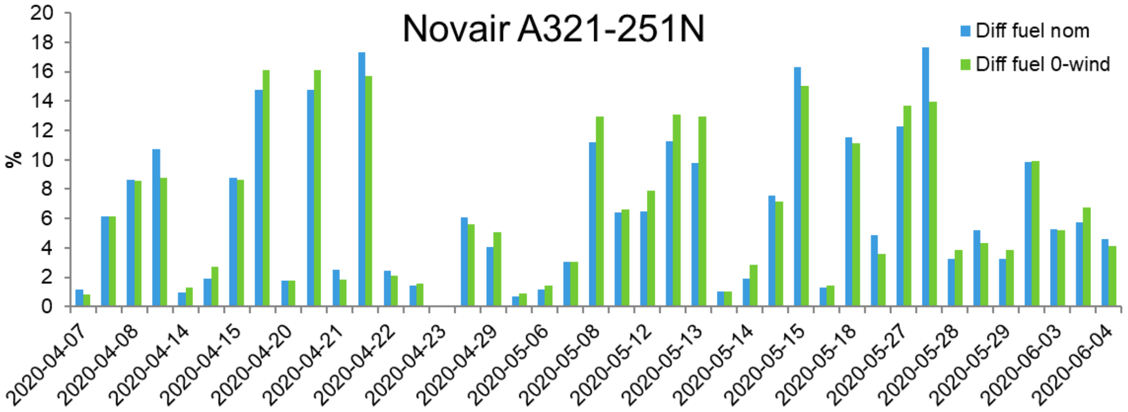

Figure 5.4. Difference in fuel consumption (%) when avoiding ice supersaturated areas on the route ARN-KRN and KRN-ARN in April-June 2020.

5.2.2 Climate optimised routes in spring 2022

For optimisation performed in spring 2022 the methodology described in section 4.6 has been used, i.e., the optimisation is based on avoidance of areas that fulfil Schmidt-Appleman criterion, are supersaturated with respect to ice, and energy forcing of the potential contrail is positive. Since the methodology was finalised to the end of the period and operative route planning with actual weather conditions was not possible, the flight routes were planned without taking winds into consideration, i.e., the so-called 'zero wind' routes, also studied during the first route climate optimisation trial. For these 'zero wind' routes, further called Nominal routes, the base case without climate optimisation is the same for all days unless some restrictions are placed in the airspace which could deviate the route. This enables to perform theoretical optimisation sensitivity studies with route planning system for other time periods but the actual weather conditions.

As the first step the total energy forcing EF_{co_r} of the flight on the Nominal route in all ISSL polygons with positive climate forcing in the way for the flight is calculated according to Equations E5 and E6. Distance flown through each ISSL polygon l_{co_p} is calculated from positions of the route and polygons. Exact position of the flight route is calculated from route plans by linear interpolation between waypoints to give instantaneous points along the route (1000 points per route). For the ARN-KRN route, these points were 0.00241942 degrees latitude apart (approximately 270 m), 0.00817818 degrees longitude apart (approximately 280 – 345 m). For the HEL-AMS route these were 0.002022022 degrees latitude apart (approximately 225 m), 0.00801702 degrees longitude apart (approximately 275 – 340 m).

For each examined day the distance flown on the route in the ISSL is calculated as the total length of route, in the horizontal plane, that intersects the ISSL polygon, starting and finishing from the closest points of the interpolated route to the ISSL polygon edges. The route that intersects the polygon in latitude and longitude is then checked to intersect in the vertical plane i.e., the flight level. Intersecting routes that are on the same flight level as the ISSL polygon edges are considered to be in ISSL. Length of the route in the ISSL polygon is calculated considering latitude and longitude only, i.e., length of its projection on horizontal plane. The total energy forcing of the flight in a polygon (EF_{co_p}, J) is calculated by multiplying the length of the route intersecting the ISSL polygon by the mean energy forcing (J/m) calculated for that ISSL polygon (E5), energy forcing of the entire flight then as sum of total energy forcing's in all polygons crossed by the flight (E6).

During the investigated three-months period (89 days) for 60% - 65% of the evening flights some polygon with potential of formation of contrails with positive energy forcing occurred in the area. However, the majority of the polygons was situated in altitudes lower than a typical cruising flight level and/or not directly in the way for the flight resulting in that only 5-10% of the polygons resulted in radiative forcing of the investigated flights. Figure 5.5 shows distribution of the ISSL polygons along the Nominal flight route ARN-KRN in the investigated period of February, March and April 2022. The greatest number of ISSL are found at the lower latitudes of the flight track, between 60 - 63° N and between flight levels 170 - 250. For this route, crossing these ISSL occurs during the ascent phase of the flight and so flight time spent inside these ISSL is likely lower than those that cross the ISSL at cruising altitudes, i.e., further north when the ascent has finished and at higher flight levels. Figure 5.6 shows an example of the flight from 2022-02-03 for the ARN-KRN route crossing ISSL that gave the greatest EF (1033 GJ) of all ISSL during the studied period. This ISSL represents not only the greatest EF, but also the longest horizontal flight route in ISSL, approximately 285 km of the 919 km route, or 31% (of the horizontal plane).

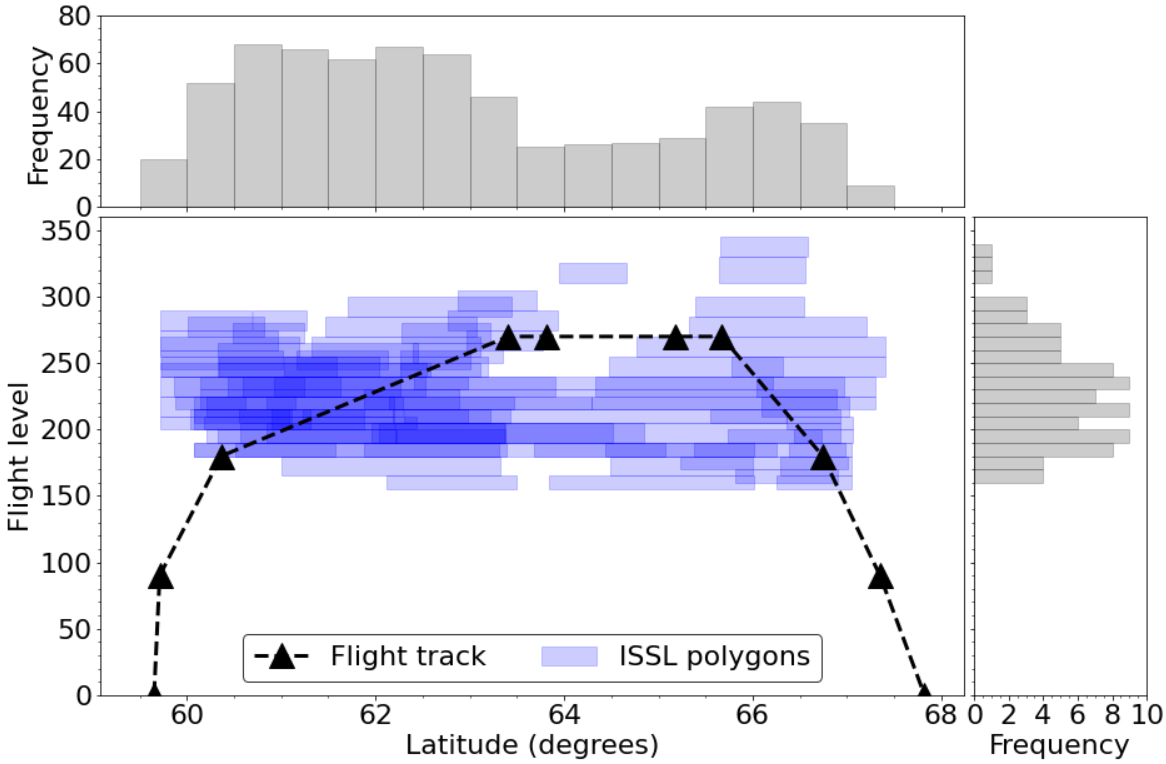

Figure 5.5. Example flight track for the ARN-KRN route (black triangles are waypoints) including representations of all ISSL polygons (n=741) from the months February, March, and April 2022. The frequency of polygon occurrence in latitude and flight levels (hundreds of feet) are also shown.

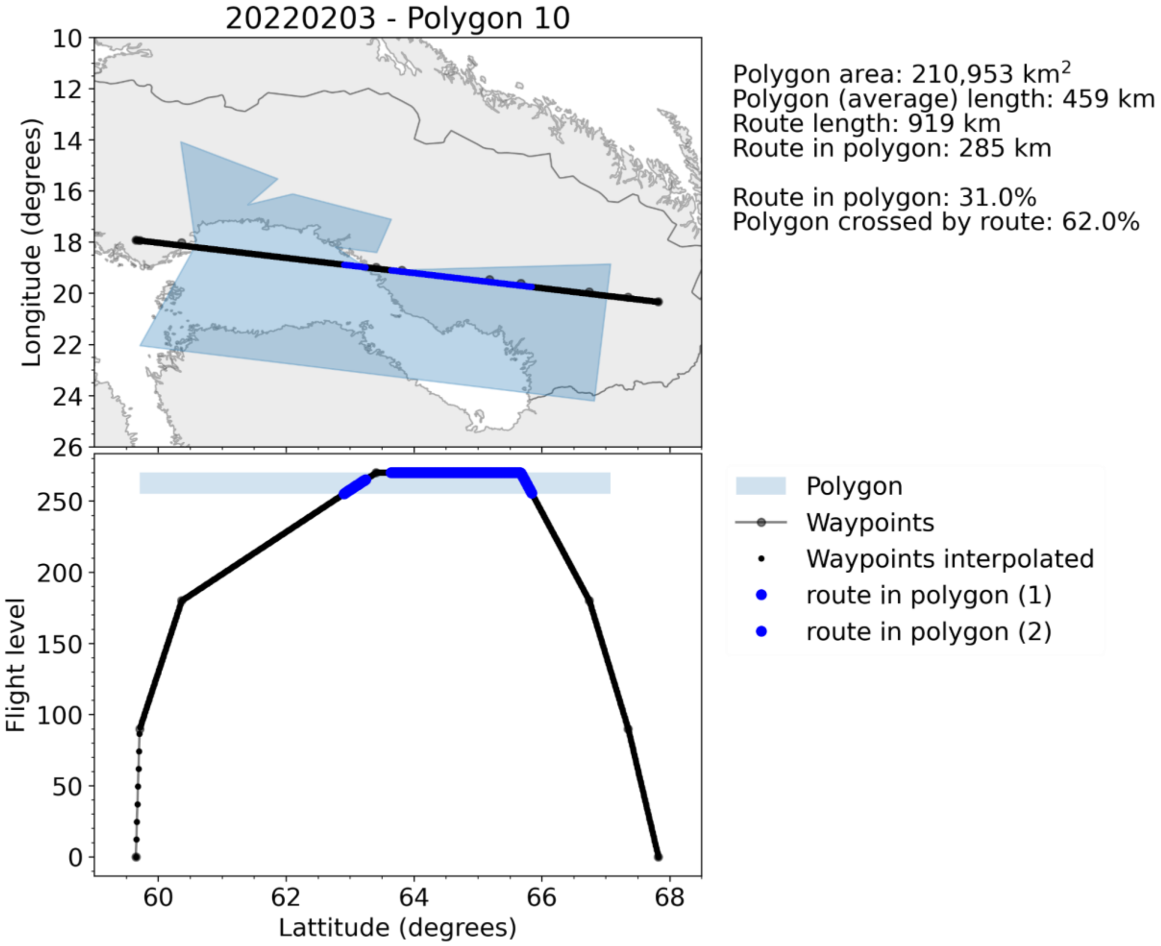

Figure 5.6. Example flight from 2022-02-03 for the ARN-KRN route crossing ISSL polygon. Top panel: top-down view of route and ISSL. Bottom panel: Vertical cross-section of route and ISSL polygon. Grey line and points are waypoints. Black points are the interpolated waypoints representing the flight route. The light blue polygon is the ISSL. Highlighted with blue dots are the points along the route that intersect the ISSL from which the EF is calculated.

The total energy forcing from contrails and contrail cirrus triggered by a flight is dependent of many parameters including the radiative conditions, water content in the ISSL layer and lifetime of the contrails and cirrus clouds as well as of the distance flown by the aircraft through the ISSL. Figure 5.7 shows scatter plot of Total energy forcing of a flight in a polygon (EFtot_p) as a function of flight route distance in ISSL polygons (l_{co_p}) and of the mean EF per metre of flight (EF_{com_x}) for the HEL-AMS and ARN-KRN routes, each point representing one flight path crossing an ISSL polygon. No correlation between the length of route in the ISSL polygon l_{co_p} and the total EF, EF_{tot_p}, suggests that flight distance in the ISSL polygon is not an important factor for producing high EFs. A strong positive correlation between mean EF_{com_x} of the ISSL and total EF_{tot_p} suggests that the intrinsic property of mean EF per metre of the ISSL polygon is an important factor controlling the ultimate magnitude of EF. As shown in section 4 important parameter for EF_{com_x} is the lifetime of the ISSL. Indeed, while l_{co_p} only affects the immediate length of a fresh, thin contrail, increasing lifetime increases the total area of the contrail in time and space where the lifetime of the contrail corresponds to lateral dimension, its expanding width as perpendicular dimension and importantly, throughout the ISSL lifetime the water vapour condensing on ice particles of the spreading contrail increases the ice water path and with that also optical depth of the contrail and contrail cirrus. Therefore, also very short flight distances leading through ISSL can cause high energy forcing.

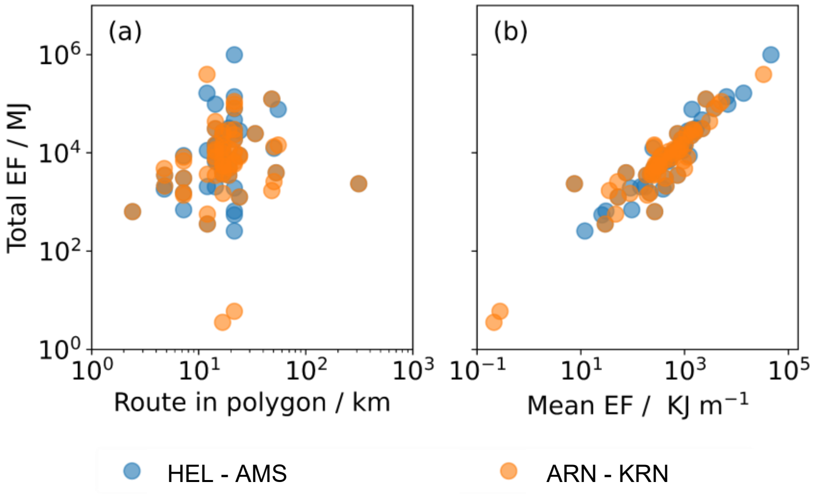

Figure 5.7. (a) Log-log scatter plot of Total energy forcing (EF_{tot_p}) as a function of flight route distance in ISSL polygons (l_{co_p}) for the HEL-AMS and ARN-KRN routes. (b) Log-log scatter plot of Total energy forcing EF_{tot_p} as a function of mean EF per metre of flight (EF_{com_x}) for the HEL-AMS and ARN-KRN routes. Each point represents one flight path crossing an ISSL polygon.

During the 89 days investigated, 30 and 17 flights caused contrail cirrus with positive energy forcing on the route ARN-KRN and HEL-AMS, respectively. In Figure 5.8 the climate impact for these flights is shown as equivalent jet-fuel mass which would cause the same energy forcing on time horizon of 20 years. To calculate the external cost of climate impact of these contrails, as a very rough estimate we use a unit cost of CO_2-equivalent emission of 50-150 $/t CO_2 (TWG US Government 2021). In total, the energy forcing caused by contrail cirrus formed on route ARN-KRN was equal to forcing of CO_2 from 5 350 kg of fuel on a 20-years horizon, which is 1.9% of total fuel consumption. The external costs of the climate forcing of the contrail cirrus was calculated to $850 - $2540. For route HEL-AMS the total energy forcing of contrail cirrus corresponded to 1 750 kg fuel and the external cost was $280 - $830. Impact of the contrail cirrus during the investigated period was 2% and 0.4% of impact of the fuel on ARN-KRN and HEL-AMS routes, respectively. On the ARN-KRN route the three flights with highest energy forcing were responsible for 63% of the total EF of the investigated flights on the route. On the HEL-AMS route the two flights with the highest energy forcing were responsible for 13%.

Figure 5.8. Kg of fuel with CO_2 emissions equivalent to EF_{co_r} (on 20-years horizon) for each flight with positive energy forcing on route HEL-AMS (upper panel) and ARN-KRN (lower panel) and the corresponding external costs of flights (assuming external cost of 1t CO_2eq = 1000 $).

Some of the flights where the route passed through ISSL polygons with positive energy forcing were re-routed to avoid them. The re-routing was performed by Novair using a flight-planning system and an A321neo aircraft. The ISSL polygons were inserted as restricted areas into the flight planning system and the re-routing was performed manually. The flight planning systems of today do not contain functionality for optimising a flight with respect to contrail formation and manually finding the best solution in the case of many ISSL polygons along the route quickly becomes quite complex. Possibilities of climate optimisation were therefore investigated only on selected examples of single ISSL polygon along the route completed with sensitivity tests of its avoidance. The sensitivity tests included avoidance in vertical direction with different changes of the flight level and one case of horizontal avoidance. True climate route optimisation would require development of a functionality for optimisation based on the ISSL polygons with their EF value or certain cost of EF caused by the flight in flight planning systems. This would require collaboration with a flight planning system supplier.

The first test of polygon avoidance was performed on the polygon depictured in Figure 5.6. In this case it covers a major part of the route at flight level (FL) 260 - 270, also close to the airport where the route cannot be altered due to the Standard Instrument Departure (SID) and Standard Arrival Route (STAR). Two alternative flight plans, avoiding the ISSL polygon, were investigated (Figure 5.9):

1. Case no 1: Route unmodified (dark grey in Fig. 5.9) but with cruise altitude restricted to maximum FL 250, hence flying below the whole ISSL polygon. The fuel consumption for this case was 280 kg (8%) higher than for the unconstrained, nominal route.
2. Case no 2: A route which slightly deviates from the nominal route (red in Fig. 5.9) passing beneath the first part of the ISSL polygon and then climbing to a flight level above FL 270 in the area outside the ISSL polygon (left of RASEN) to pass above the last part of the polygon. The fuel consumption for this case was 150 kg (5 %) higher than for the unconstrained, nominal route.

The total energy forcing EF_{co_r} of the nominal flight through this polygon is 1 TJ which corresponds to forcing of CO_2 from 820 kg fuel on 20-years horizon. In Fig. 5.8 we can see that on route ARN-KRN there are 3 more days where EF_{co_r} corresponded to EF from more than 500 kg fuel.

In addition, flight plans with cruising altitude restricted to different flight levels during the entire cruise were calculated as well as for a modified route on optimal altitude with longer flight distances simulating horizontal avoidance of polygons. Table 5.1 shows additional fuel used, distance flown, and time of the deviating flight compared to the nominal one. These results need to be seen as examples relating the specific case that was studied (altering a particular route with the particular aircraft used and the conditions selected).

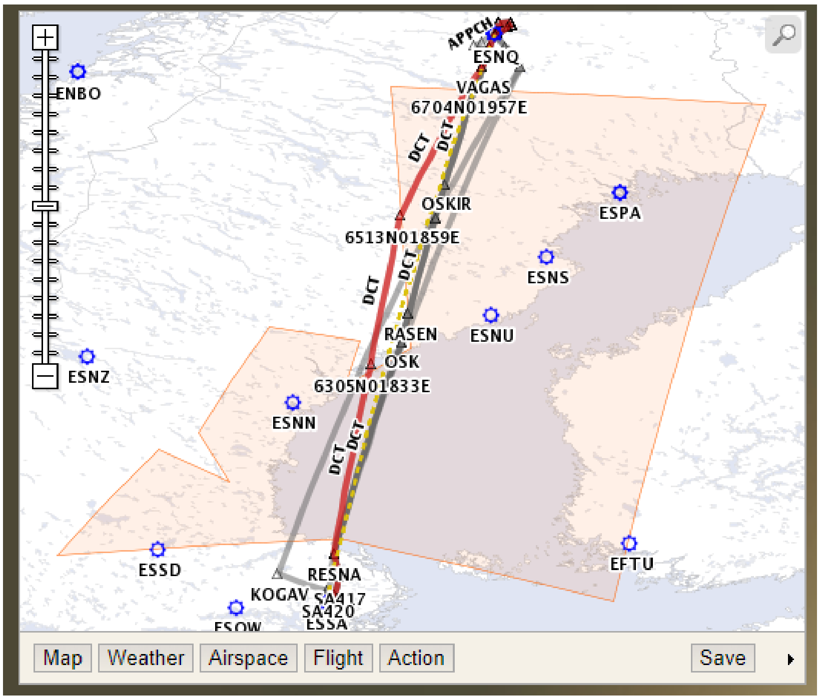

Figure 5.9. Nominal and alternative flight routes avoiding the ISSL polygon between ARN-KRN (ICAO codes ESSA-ESNQ used in the figure). Dark grey – nominal route; Yellow dashed line – great circle; Light grey – Routes with free flight altitude and horizontal avoidance of the polygon.

Table 5.1. Parameters of the nominal route ARN-KRN and alternative routes on lower flight levels or/and with horizontal avoidance for aircraft A321neo.

	Flight distance	Cruising FL	Fuel consumed	Additional fuel		Additional distance
	(km)	(100 feet)	(kg)	(kg)	(%)	(%)
Nominal route ARN-KRN	**524**	**380**	**3 139**	**-**	**-**	**-**
Case no. 1	524	250 & 240	3 416	277	8.8%	-
Case no. 2	524	240 & 360	3 297	158	5.0%	-
FL 360	524	360	3 145	6	0.2%	-
FL 340	524	340	3 174	35	1.1%	-
FL 320	524	320	3 206	67	2.1%	-
FL 300	524	300	3 260	121	3.9%	-
FL 280	524	280	3 298	159	5.1%	-
FL 260	524	260	3 360	221	7.0%	-
FL 240	524	240	3 486	347	11.1%	-
+10 NM	534	380	3 200	61	1.9%	1.9%
+23 NM	547	380	3 276	137	4.4%	4.4%
+47 NM	571	380	3 402	263	8.4%	9.0%

The second test of ISSL avoidance was performed for route HEL-AMS. The nominal route and the horizontal-avoidance route are shown in Figure 5.10. Vertical avoidance through decrease of the cruising altitude by different flight level has been tested as well and results in terms of additional fuel burned and additional distance flown are shown in Table 5.2. While horizontal avoidance of the example polygon resulted in 30% additional fuel used the maximum fuel penalty on vertical avoidance was 4 % of fuel (220 kg).

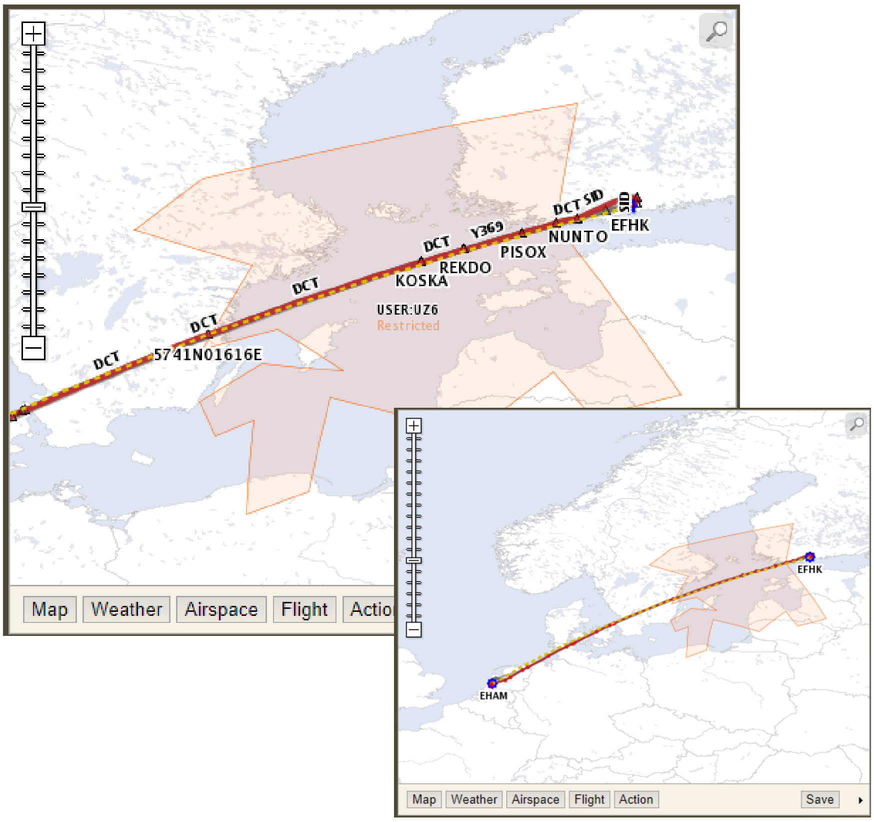

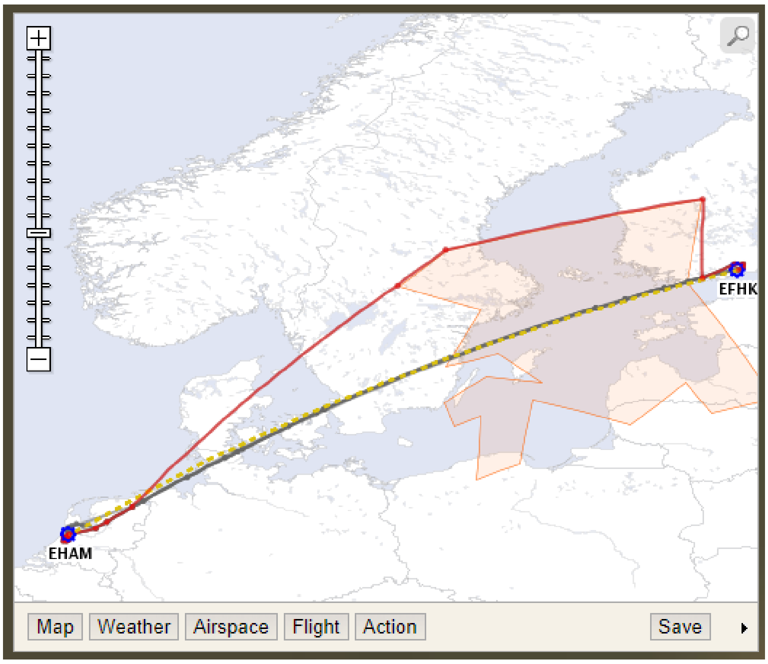

Figure 5.10. Nominal rout of flight HEL-AMS (ICAO codes EFHK-EHAM used in the figure, upper 2 panels) and alternative flight routes avoiding the ISSL polygon in horizontal direction (bottom panel, red line). Dashed line – great circle.

Table 5.2. Parameters of the nominal route HEL-AMS and alternative routes on lower flight levels or/and with horizontal avoidance for aircraft A321neo.

	Flight distance	Cruising FL	Fuel consumed	Additional fuel		Additional distance
	(km)	100 feet	(kg)	(kg)	(%)	(%)
Nominal route HEL-AMS	**879**	**360**	**5 186**			
Horizontal avoidance	1 119	340 & 240	6 930	1 744	33.6%	27.3%
FL 340	879	340	5 212	26	0.5%	-
FL 320	879	320	5 232	46	0.9%	-
FL 300	879	300	5 261	75	1.4%	-
FL 280	879	280	5 322	136	2.6%	-
FL 260	879	260	5 409	223	4.3%	-

6 Conclusions and future perspectives

The OP-FLYKLIM project investigated the potential to reduce the climate impact of aviation through climate optimization of flight routes to reduce the high-altitude effects of aviation with a focus on climate forcing from contrails and contrail cirrus under Scandinavian conditions. Several aspects of contrail formation were investigated during the project.

Important conditions for formation of contrails are the existence of regions in the atmosphere that are ice supersaturated and free of clouds. OP-FLYKLIM has investigated the climatology of such areas over Scandinavia in output data from meteorological models and found them rather frequent. Comparison of relative humidity over ice according to two different models, ECMWF's model IFS and MetCoOP's model AROME with observations showed that the models tend to underestimate ice supersaturation. Also, comparison of ice supersaturation modelled by the AROME model with observations of contrails performed by SMHI within OP-FLYKLIM indicated underprediction of ice supersaturated regions by the model.

In aviation meteorological forecasts of good quality are important for flight planning as well as for studies of climate impact. At the same time Mode-S EHS data on winds and temperature in the upper atmosphere sent from aircrafts can be used by the meteorological models to improve their performance. In OP-FLYKLIM a test of streaming of these data to SMHI operational forecast model was performed and showed good results.

OP-FLYKLIM has developed a methodology to identify ice-supersaturated layers in defined regions and to calculate climate impact of contrails potentially formed in these ISSL. This methodology is relatively simple and builds on open-source operational meteorological data which makes it quite promising. To test the methodology for climate route optimisation, the ISSL polygons need to be defined as areas with certain cost or other value that can be used by a flight planning system to optimise for climate impact caused by contrails. Such optimisation functionality is not available in the flight planning systems today but need to be implemented together with a flight planning system supplier. In such a project, it would also be beneficial to include an Airspace User (airline) and an Air Navigation Service Provider.

The climate impact of contrails and contrail cirrus triggered by a flight was calculated as total energy forcing during their entire lifetime. This energy forcing can also be expressed as CO_2 equivalents and related equivalent mass of jet fuel. OP-FLYKLIM has evaluated the impact of individual flights during a three-month period, ca. 180 evening flights on two routes. For the majority of the evening flights some polygon with potential of formation of contrails with positive energy forcing occurred in the area, however, only 5-10% of the polygons resulted in radiative forcing of the investigated flights as the majority of the polygons was not crossed by the flight route. Impact of the contrail cirrus for the investigated flights was 2% and 0.4% of impact of the fuel on ARN-KRN and HEL-AMS routes, respectively. While the impact of the majority of flights was small, few flights had high energy forcing exceeding the impact of the fuel burned on the flight. This finding is in agreement with findings of Teoh et al. (2020) who calculated that 2.2% of flights over Japan contribute to 80% of the contrail EF in this region.

The OP-FLYKLIM tests performed has also shown directions for improvements to be made:

- Air humidity and its water vapour saturation with respect to ice is a critical parameter for calculation of the energy forcing of contrail cirrus. Results of this study based on literature review as well as on own results indicate that the models tend to underestimate ice supersaturation. Sensitivity of the method for calculation of the energy forcing of the contrail cirrus to several ice super-saturation fields therefore needs to be investigated.

- Quantification of the energy forcing of the flight needs to be investigated for a much larger number of situations regarding the length of the investigated period, time of the day, types of aircraft and lengths of flights. As a start, all investigated ISSL polygons from 2020 and 2022 trials could be analysed for several aircraft types. Further study requires availability of a wider dataset of route plans or FDR data. For future investigations also the ISSL polygons need to be defined in a way that they cover regions with homogeneous properties regarding the evolving contrail cirrus which requires further study of variability of properties of seeds within the ISSL polygons.

Acknowledgments

Karl-Ivar Ivarsson at SMHI is gratefully acknowledged for performing the evaluation of the ECMWF and AROME models with observed supersaturation over ice from radiosondes as well as for evaluating simulations with standard and modified versions of the AROME forecast model for cases with observed contrails in 2020. Christian Asker at SMHI is gratefully acknowledged for developing code to delineate polygons of ice supersaturated regions based on operational weather model forecasts. Peter Björklund at Novair is gratefully acknowledged for assistance with the climate route optimization involving Novair’s flight planning system.

References

Björklund, E., 2011. Observed Ice Supersaturated Layers over Sweden and Implications for Aviation Induced Contrails over the Baltic Sea, Uppsala university, ISSN 1650-6553 ; 220.

Dee, D.P., Uppala, S.M., Simmons, A.J., Berrisford, P., Poli, P., Kobayashi, S., Andrae, U., Balmaseda, M.A., Balsamo, G., Bauer, P., Bechtold, P., Beljaars, A.C.M., van de Berg, L., Bidlot, J., Bormann, N., Delsol, C., Dragani, R., Fuentes, M., Geer, A.J., Haimberger, L., Healy, S.B., Hersbach, H., Holm, E.V., Isaksen, L., Kållberg, P., Kohler, € M., Matricardi, M., McNally, A.P., Monge-Sanz, B.M., Morcrette, J.-J., Park, B.-K., Peubey, C., de Rosnay, P., Tavolato, C., Thepaut, J.-N., Vitart, F. (2011). The ERA-Interim reanalysis: configuration and performance of the data assimilation system. Q. J. R. Meteorol. Soc. 137 (656), 553–597. https://doi.org/10.1002/qj.828.

Grewe V. et al., 2014. Aircraft routing with minimal climate impact: the REACT4C climate cost function modelling approach (V1.0). Geosci. Model Dev. 7, 175–201

Grewe, V.; Dahlmann, K.; Flink, J.; Frömming, C.; Ghosh, R.; Gierens, K.; Heller, R.; Hendricks, J.; Jöckel, P.; Kaufmann, S.; et al. Mitigating the Climate Impact from Aviation: Achievements and Results of the DLR WeCare Project. Aerospace **2017**, 4, 34.

Hersbach, H.; Bell, B.; Berrisford, P.; Biavati, G.; Horányi, A.; Muñoz Sabater, J.; Nicolas, J.; Peubey, C.; Radu, R.; Rozum, I.; et al. ERA5 Hourly Data on Pressure Levels from 1979 to Present. Copernicus Climate Change Service (C3S) Climate Data Store (CDS). Available online: https://cds.climate.copernicus.eu/cdsapp#!/dataset/10.24381/cds.bd0915c6?tab=overview (accessed on 18 July 2022).

IPCC, 1999. Aviation and the global atmosphere. In: E Penner, J., Lister, D.H., Griggs, D.J., Griggs, D.J., Dokken, D.J., McFarland, M. (Eds.), Intergovernmental Panel on Climate Change. Cambridge University Press, Cambridge, UK.

IPCC, 2013. Climate Change 2013: The Physical Science Basis. Contribution of Working Group I to the Fifth Assessment Report of the Intergovernmental Panel on Climate Change [Stocker, T.F., D. Qin, G.-K. Plattner, M. Tignor, S.K. Allen, J. Boschung, A. Nauels, Y. Xia, V. Bex and P.M. Midgley (eds.)]. Cambridge University Press, Cambridge, United Kingdom and New York, NY, USA, 1535, **2013**.

Jacobsson, M. Z., Wilkerson, J. T., Balasubramanian, S., Cooper, W. W. Jr., Mohleji, N., 2012. The effects of rerouting aircraft around the arctic circle on arctic and global climate. Climate Change 115, 709-724.

Kärcher, B., Mahrt, F., Marcolli, C. (2021). Process-oriented analysis of aircraft soot-cirrus interactions constrains the climate impact of aviation. Commun. Earth Environ. 2, 113.

Lee, D.; Fahey, D.; Forster, P.; Newton, P.; Wit, R.; Lim, L.; Owen, B.; Sausen, R. Aviation and global climate change in the 21st century. Atmos. Environ. **2009**, 43, 3520–3537.2.

Lee, D.; Fahey, D.; Skowron, A.; Allen, M.; Burkhardt, U.; Chen, Q.; Doherty, S.; Freeman, S.; Forster, P.; Fuglestvedt, J.; et al. The contribution of global aviation to anthropogenic climate forcing for 2000 to 2018. Atmos. Environ. **2020**.

Marenco, A.; Thouret, V.; Nedelec, P.; Smit, H.; Helten, M.; Kley, D.; Karcher, F.; Simon, P.; Law, K.; Pyle, J.; et al. Measurement of ozone and water vapor by Airbus in-service aircraft: The MOZAIC airborne program, An overview. J. Geophys. Res. **1998**, 103, 25631–25642.

Meyers et al 1992 : New primary ice-nucleation parameterization in an explicit cloud model J. Appl. Meteor. 31, 708-721

Mårtensson, T. and Hasselrot, A. Beräkning av avgasemissioner från flygtrafik – FOI. FOI-R-3677—SE, **2013**.

EASA, ICAO's engine exhaust emission database, **2021**.

Tomas Mårtensson, Therese Sjöberg och Patrik Bergviken. Inrikesflygets klimatpåverkan – en analys av radarspår, . TSA-2016-122, **2016**.

Technical Working Group on Social Cost of Greenhouse Gases, US government. Technical Support Document: Social Cost of Carbon, Methane, and Nitrous Oxide Interim Estimates under Executive Order 13990. **2021**. https://www.whitehouse.gov/wp-content/uploads/2021/02/TechnicalSupportDocument_SocialCostofCarbonMethaneNitrousOxide.pdf, assessed 2022-06-05.

Petzold, A., Neis, P., Rütimann, M., Rohs, S., Berkes, F., Smit, H. G. J., Krämer, M., Spelten, N., Spichtinger, P., Nédélec, P., and Wahner, A.: Ice-supersaturated air masses in the northern mid-latitudes from regular in situ observations by passenger aircraft: vertical distribution, seasonality and tropospheric fingerprint, Atmos. Chem. Phys., 20, 8157–8179, https://doi.org/10.5194/acp-20-8157-2020, **2020.**

Schumann, U. On conditions for contrail formation from aircraft exhausts. Meteorol. Z. **1996**, 5, 4–23.

Schumann, U. A contrail cirrus prediction model, Geosci. Model Dev., 5, 543–580, **2012**, www.geosci-model-dev.net/5/543/2012/doi:10.5194/gmd-5-543-2012.

Schumann, U., Mayer, B., Graf, K., Mannstein, H. A Parametric Radiative Forcing Model for Contrail Cirrus. J. Applied Meteorology and Climatology 51, 1391–1406, **2012**, DOI: 10.1175/JAMC-D-11-0242.1.

Schumann, U.; Heymsfield, A. On the lifecycle of individual contrails and contrail cirrus. Meteorol. Monogr. **2017**, 58, 3.1.

Sherwood, S. C., Bony, S., Boucher, O., Bretherton, C., Forster, P. M., Gregory, J. M. and Stevens, B. (2015). Adjustments in the forcing-feedback framework for understanding climate change. Bulletin of the American Meteorological Society, 96, pp. 217-228. doi: https://doi.org/10.1175/BAMS-D-13-00167.1.

Teoh, R.; Schumann, U.; Majumdar, A.; Stettler, M. Mitigating the climate forcing of aircraft contrails by small-scale diversions and technology adoption. Environ. Sci. Technol. **2020**, 54, 2941–2950.

SMHI

FOI

LFV

Swedavia
Airports

novair

TRAFIKVERKET

TRANSPORT
STYRELSEN

ivl

IVL Swedish Environmental Research Institute Ltd.
P.O. Box 210 60 // S-100 31 Stockholm // Sweden
Phone +46-(0)10-7886500 // www.ivl.se